Soil pore water evaporation and temperature influences on clay mineral paleothermometry

Daniel E. Ibarra[1,2] and Jaivime Evaristo[3]

1. Institute at Brown for Environment and Society, Brown University, Providence, RI, 02906 USA
2. Department of Earth, Environmental and Planetary Science, Brown University, Providence, RI, 02906 USA
3. Copernicus Institute of Sustainable Development, Utrecht University, Utrecht, The Netherlands

Corresponding author: Daniel E. Ibarra; daniel_ibarra@brown.edu

Abstract

Clay mineral isotope paleothermometry is fundamental to understanding Earth's climate system and landscape evolution. Status quo methods, however, assume constant factors, such as temperature and water isotopic compositions, and ignore seasonality, soil water evaporation and depth dependent temperature changes. We propose first-order modifications to address these factors and test them in a modeling framework using published data from various settings. Our forward model reveals that neglecting evaporation and temperature variability may lead to significant underestimations of clay formation temperatures, especially in Mediterranean settings. Our inverse model indicates that high-latitude Eocene clay formation temperatures were ~8°C warmer than modern, while Eocene river sediments in the Sierra Nevada show evaporation-influenced trends, suggesting that previous paleoelevation estimates were underestimated. Our framework demonstrates that explicit consideration of soil pore water evaporation and temperature variability is necessary when interpreting clay mineral isotope data in the context of temperature, hydroclimate and elevation reconstructions.

Introduction

Stable oxygen and hydrogen isotope methods are valuable tools for understanding Earth's system processes, such as temperature fluctuations and changes in the water cycle[1-5]. These methods rely on the isotopic fractionation that occurs during phase changes in the water cycle[6-10] and the equilibrium precipitation of minerals from surface waters preserved in geologic records[11-13]. However, few geologic records capture both oxygen and hydrogen stable isotope ratios in the same phase. To address this issue, researchers developed fluorination and pyrolysis methods for measuring oxygen and hydrogen stable isotope ratios in clay minerals in the 1970s[14,15].

In the field of clay mineral thermometry, scientists have used clay minerals as single mineral thermometers or in combination with other mineral phases to study terrestrial paleoclimate and paleoaltimetry[16-34]. Similar approaches have been applied to marine and lacustrine cherts[35-38], and iron oxides[39-40].

In the field of stable isotope hydrology, the global meteoric water line (GMWL $\delta^2H = 8x\delta^{18}O + 10$) serves as the starting point for understanding hydrological processes[3,5,6]. Recent studies have considered the role of evaporated soil waters in both field and modeling studies [42-46]. However, the impact of evaporated soil waters on clay mineral thermometry has not been extensively examined in a systematic fashion (cf. ref. 27). Conversely, the implications of the temperatures and isotopic compositions at which clays form within the framework of evaporated soil waters in hydrology and weathering studies remain unexplored. Together with developments in analytical laboratory capabilities, an integrated framework between the fields of clay mineral thermometry and stable isotope hydrology could yield new tools for understanding clay formation processes in modern weathering profiles. But, to our knowledge, no such explicit attempts have been made. Here, we propose a cross-disciplinary approach between these two fields. We reevaluate key assumptions in both fields and suggest a refined methodology for interpreting clay mineral stable isotope datasets from past and present weathering profiles. We do so by incorporating recent advances in critical zone water stable isotope systematics[5,43-45].

In the following we begin by reviewing the common thermometry assumptions used when interpreting clay mineral D/H and $^{18}O/^{16}O$ variations in modern and paleo-weathering

profiles. Next, we develop theories that account for the following three factors as first-order modifications to the status quo method: 1) co-variations in the seasonality of temperature and the isotopic composition of meteoric waters along the local meteoric water line (LMWL); 2) the role of pore water evaporation trends away from the LMWL; and 3) the impact of seasonal soil temperature variations with depth. Our point of departure is that these factors are important for, and relatively well constrained in, describing broad patterns across modern weathering and paleo-weathering datasets. Finally, as an example of our approach we test our developed theories within a modeling framework that calculates clay $\delta^{18}O$ and $\delta^{2}H$ using measured soil pore water $\delta^{18}O$ and $\delta^{2}H$ (forward model), and vice versa (inverse model).

What is the status quo?

Isotopic fractionation of oxygen and hydrogen during clay mineral precipitation is valuable for thermometry applications. What we collectively describe here as the *status quo* method is extensively documented in previous studies[14,47-49,18,27,29]. Importantly, due to vapor pressure differences of water isotopologues, the fractionation factor ($\alpha_{clay\text{-}water} = R_{clay}/R_{water}$) of hydrogen between clays and water is less than unity at Earth surface temperatures. This results in clay minerals being more depleted in $\delta^{2}H$ than the isotopic composition of their putative source waters. The fractionation factor for oxygen, however, is greater than unity, resulting in isotopically enriched clay mineral $\delta^{18}O$ (see ref. 47 for further discussion). Together, the result is that clay minerals in equilibrium with waters during weathering and soil formation fall below and to the right of waters from which they form in $\delta^{18}O$-$\delta^{2}H$ cross plots (Box 1).

The simplicity of the status quo method has allowed researchers to infer mineral formation temperatures (gray lines parallel to LMWL, Box 1), which in turn, have been used to back-calculate the isotopic compositions of the putative 'source water'. That is, the meteoric water from which the clay mineral would have formed. As such, the location of an inferred source water on the LMWL, alternatively the GMWL, informs an interpretation regarding the elevation, temperature and paleoenvironment associated with mineral formation (Box 1). Clay minerals $\delta^{18}O$ and $\delta^{2}H$, therefore, have been used as geochemical proxies in paleoclimate and paleoaltimetry research.

Box 1: The temperature-dependence of hydrogen and oxygen fractionation between clays and water

Temperature-dependent fractionation factors require an assumption about the covariation of $\delta^{18}O$ and $\delta^{2}H$ in source waters. Historically, this covariation has been assumed to be consistent with the LMWL or GMWL[18,27,29,47,48],. This assumption creates a system with three equations and three unknowns. Solving this system uses previously determined, mineral-specific fractionation factors[12,47,65,104]. This results in characteristic monotonic relationships in the form of $1000\ln\alpha$ versus $1/T$ or $1/T^2$ at different temperatures (clay lines and temperatures, respectively, in the figure).

By using the GMWL as a key constraint, previous researchers established single-mineral thermometer relationships between temperature and measured $\delta^{18}O$ and $\delta^{2}H$ of clay minerals. For example, the empirically derived kaolinite fractionation factors determined by ref. 48 for oxygen is:

$$1000 \times \ln {}^{18}\alpha_{kaol\text{-}water} = 2.76 \times 10^{6} \times T^{-2} - 6.75 \quad (1)$$

and for hydrogen is:

$$1000 \times \ln {}^{2}\alpha_{kaol\text{-}water} = -2.2 \times 10^{6} \times T^{-2} - 7.7 \quad (2)$$

Combining these equations with the GWML ($\delta^2H = 8 \times \delta^{18}O + 10$) results in a single mineral thermometry equation as presented by ref. 29:

$$3.0350 \times 10^{6} T^{-2} = \delta^{18}O_{kaolinite} - 0.1250 \times \delta^{2}H_{kaolinite} + 7.0375 \quad (3)$$

Ref. 47 presented an analogous relationship for smectite:

$$3.54 \times 10^{6} T^{-2} = \delta^{18}O_{smectite} - 0.125 \times \delta^{2}H_{smectite} + 8.95 \quad (4)$$

In the case of kaolinite, solving for Equations 1-3 results in an array of clay minerals that would have formed at different temperatures (clay lines and temperatures in the figure). The status quo method, however, assumes that clay minerals form from waters that covary along the GMWL, and fractionate at the mean annual temperature of a given location. Thus, a given array of measured $\delta^{18}O$ and $\delta^{2}H$ of kaolinite would invariably correspond to a source water that plots on the GMWL. A source water that is enriched in the heavy isotopes (i.e., more positive δ value) informs an interpretation that the mineral must have formed under characteristic climatological (e.g., high temperature) and topographic (e.g., low elevation) conditions (red filled circle on GMWL). Similarly, a source water that is depleted in the heavy isotopes (i.e., more negative δ values) informs an interpretation that the mineral must have formed under characteristic climatological (e.g., low temperature) and topographic (e.g., high elevation) conditions (blue filled circle on GMWL).

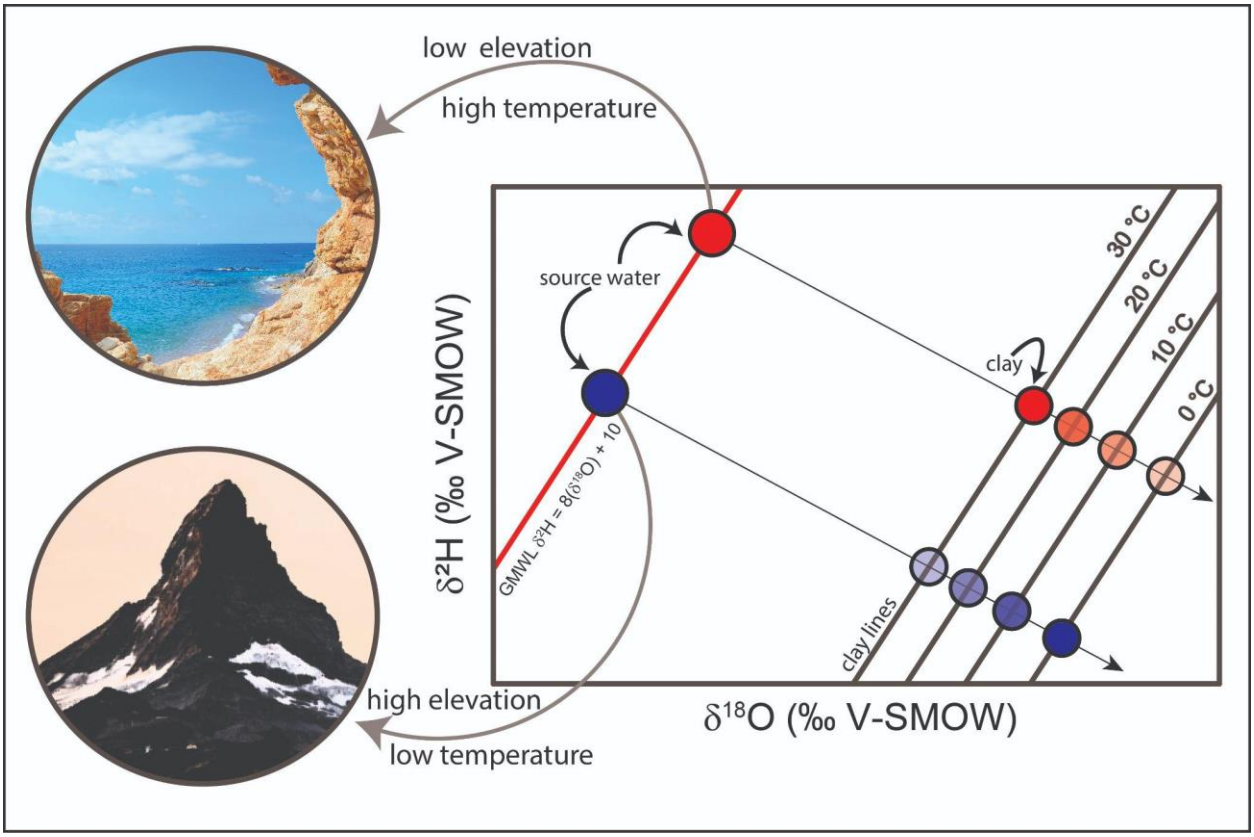

[Box 1 ends here]

What is wrong with the status quo?

Notwithstanding the simplicity of the status quo method, it invokes several key assumptions that may or may not be applicable in all settings. Firstly, the method assumes complete isotopic exchange of oxygen and hydrogen during weathering reactions. This assumption may only be plausible at high molar water/rock ratios[50,51] (other complications on the proxy fidelity of the method are detailed in the Supplemental Information). Secondly, the status quo method assumes that clay minerals form from waters that covary along the GMWL, or LMWL, and fractionate at the mean annual temperature of a given location. Previous studies, however, have shown that individual studies across different times and locations violate this assumption. That is, rather than clays (e.g., kaolinite and smectite) falling along slopes of ~8, many studies demonstrated $\delta^{18}O$ versus $\delta^{2}H$ arrays that were either steeper or shallower than expected[18,22,20,21,27,29]. Ref. 27 proposed a graphical framework for interpreting the effects of aridity and mean temperature changes. These effects, however, have not been formally tested within the framework of single-mineral clay thermometer calculations.

Further, previous work has not considered seasonal variability in the isotopic compositions of meteoric waters and temperature in greater detail. Thus, in the following we develop new theories [essentially 'thought experiments'] exploring the impact of several confounding factors on clay $\delta^{18}O$-$\delta^{2}H$ arrays. Our thought experiments, organized as cases in increasing complexity, take into account the following: 1) the role of seasonal co-variations of temperature and meteoric water isotopic composition; 2) the role of evaporatively enriched soil waters; and, 3) the role of seasonal soil temperature variability with depth.

Case 1. The role of seasonal co-variations of temperature and meteoric water isotopic composition

The amount and isotopic composition of precipitation co-vary both positively and negatively on a seasonal basis with temperature across Earth's land masses[5]. Such variations are generally set by changing precipitation regimes as a function of latitude such as monsoonal versus synoptic precipitation delivery[2,52,53]. For example, $\delta^{18}O$ and $\delta^{2}H$ of precipitation decrease during tropical summers due to the 'amount effect' dominating monsoon rainfall[5]. This leads to negative covariation between temperature and the $\delta^{18}O$ and $\delta^{2}H$ values of precipitation. Conversely, in mid- to high-latitudes, changes in moisture source, humidity and temperature of precipitation typically lead to a positive covariation between temperature and $\delta^{18}O$ and $\delta^{2}H$ values of precipitation, with the most depleted values occurring during the winter. In mediterranean climates on the west side of major continents, winters also often correspond to the wet season. In the subsequent hypothetical calculations shown below, we isolate the impact of seasonal positive and negative covariation between temperature and the isotopic composition of precipitation with respect to the single-mineral clay thermometers presented in equations 1 and 2 (cf. ref. 48).

Case 2: The role of evaporatively enriched soil waters

Some of the precipitation water that infiltrates the soil may evaporate, leading to an enrichment of heavy isotopes in the remaining soil water due to kinetic fractionation. That is, the preferential transport of lighter water isotopologues away from a liquid source during evaporation (i.e., $H_2{}^{16}O > HD^{16}O > H_2{}^{18}O$). As a result, the relationship between $\delta^{18}O$ and $\delta^{2}H$ for water subjected to evaporation will diverge from the GMWL. Ref. 53 defined the divergence from GMWL as deuterium excess (*d*-excess = $\delta^{2}H - 8x\delta^{18}O$). This means that the smaller the *d*-excess value the larger is the effect of evaporation on a water sample.

A meta-analysis of 65 peer-reviewed papers between 1990 and 2017 showed a systematic increase in the median *d*-excess of soil waters with soil depth across climate types[42]. This suggests that soil waters close to the surface tend to experience more evaporation than soil waters in deeper parts of the soil profile[54]. Furthermore, in a $\delta^{18}O$-$\delta^{2}H$ cross plot, it was predicted[55] that the evaporation slopes of soil water globally range between 2 and 3. This range is much shallower than the 4-5 range of evaporation slopes for lakes and agrees with available data at the time. The 2-3 range of evaporation slopes for soils also approximates the 3.1-3.4 range in a later modeling study[44]. In this study, we examine the influence of modern evaporated soil waters on clay mineral thermometry. We focus on soil evaporation slopes between 2 and 3, as this approach avoids assuming that all evaporated soil water samples come from a single source[44]. As a result, we can determine the isotopic compositions during clay formation without the need to extrapolate the intersections of modern soil water samples with the LMWL.

To model soil pore water evaporation, we implement the model described by ref. 56 for steady state evaporation and diffusion. Our application of the ref. 56's model follows that of ref. 57 who modeled soil carbonate $\delta^{18}O$ in semiarid regions. The following equation describes an asymptotic relationship with depth (z_i) between the amount weighted average precipitation value ($\delta^{18}O_{precipation}$) with a surface soil water value ($\delta^{18}O_{surface}$) set by an assumed soil evaporation slope and seasonal precipitation $\delta^{18}O$ and $\delta^{2}H$ variation[56]:

$$\delta^{18}O_i = (\delta^{18}O_{surface} - \delta^{18}O_{precipitation}) \times (\exp(-z_i/z^*)) + \delta^{18}O_{precipitation} \quad (5).$$

The decrease in $\delta^{18}O$ and $\delta^{2}H$ with depth is caused by the upward wicking of water as the soil dries. The decrease in $\delta^{18}O$ and $\delta^{2}H$ with depth is a function of a characteristic decay length (z^*) that is set by the evaporation rate, effective diffusivity, tortuosity and porosity of a soil profile[56-59]. In the calculations presented below, we solve equation 5 on a monthly basis for our hypothetical arrays. We assume evaporation slopes of between 2 and 4, while varying precipitation $\delta^{18}O$ and $\delta^{2}H$ seasonally. We then solve equation 5 for wet and dry seasons in our data-model comparison using modern field measurements.

Case 3: The role of seasonal soil temperature variations with depth

In addition to the complication that depth trends in pore water $\delta^{18}O$ and $\delta^{2}H$ composition imposes, the isotopic composition of authigenic soil minerals (i.e., minerals that form as a result of *in situ* processes within the soil environment) records the soil temperature at the time in which those minerals precipitate, not the instantaneous or annual average air temperature. An analogous example includes recent studies focused on carbonate clumped isotope signatures (Δ_{47}) of soil carbonates, which have noted the potential bias in soil carbonate formation temperatures whereby soil temperatures recorded by carbonates may be warmer than annual or seasonal air temperatures due to radiative heating effects[60-63]. Nonetheless, clay minerals in weathering profiles and soils are likely less seasonally biased than carbonates, a fact that has been previously leveraged when measured together with carbonates in the same profile and/or stratigraphic sections and time intervals[30,31,34]. Seasonal (and daily) air temperature variability is damped and lagged with depth in the soil column using a heat diffusion equation at a given depth (z) and time (t)[64]:

$$T_{z,t} = T_{avg} + A_o[\sin(\omega t - z/d)]/e^{z/d} \quad (6),$$

where T_{avg} is the mean annual air temperature, A_o is the seasonal amplitude, ω is radial frequency (2π/year), and d is the damping depth. The damping depth is a function of the thermal conductivity and volumetric heat capacity of the soil[61,64]. Recently, ref. 59 estimated an average value of 153 cm based on typical thermal conductivity and heat capacity values. In this work, for the theoretical and applied calculations presented below, we follow ref. 59 and assume a damping depth of 153 cm and implement equation 6 monthly for our hypothetical arrays, and seasonally for our data-model comparison.

Applications

In the next section, we present simulation results obtained by implementing our three conceptual models, Cases 1-3. We then test the validity of these models with data from modern and paleo soil water datasets. We refer to the models that underpin our data-model comparisons as forward and inverse models. The *forward* model uses modern soil water $\delta^{18}O$ and $\delta^{2}H$ data ($\delta^{18}O_{sw}$ and $\delta^{2}H_{sw}$, respectively) as input to generate $\delta^{18}O$ and $\delta^{2}H$ values of kaolinite ($\delta^{18}O_{kaol}$ and $\delta^{2}H_{kaol}$, respectively) as output:

$$\delta^{18}O_{kaol} = \delta^{18}O_{sw} + 1000\ln{}^{18}\alpha_{kaol\text{-}water} \quad (7)$$

$$\delta^{2}H_{kaol} = \delta^{2}H_{sw} + 1000\ln{}^{2}\alpha_{kaol\text{-}water} \quad (8)$$

where the second terms in Equations (7) and (8) are the same as in Equations (1) and (2). We underline that these calculations, following ref. 65,, assume that 1000lnα is the difference between the water and clay mineral composition, which is a commonly used approximation. The inaccuracy introduced by this approximation is comparatively minor, less than 2 °C depending on the initial composition of the source water and the temperature of clay formation. The *forward* model seeks to answer the question: Given $\delta^{18}O_{sw}$ and $\delta^{2}H_{sw}$ measurements, resulting from relatively well-constrained processes that lead to a sample plotting on or below the LMWL, to what extent can the calculated $\delta^{18}O_{kaol}$ and $\delta^{2}H_{kaol}$ agree or disagree either with the status quo method or any of the model conceptualizations (Cases 1-3)? We implement the forward model at two locations: one at a low-latitude site in Luquillo, Puerto Rico[66], and another at a mid-latitude site in Oregon[67].

Conversely, the *inverse* model uses $\delta^{18}O_{kaol}$ and $\delta^{2}H_{kaol}$ data to predict the plausible values of $\delta^{18}O_{sw}$ and $\delta^{2}H_{sw}$ that best explain the observed kaolinite observations. The inverse model seeks to answer the question: Given $\delta^{18}O_{kaol}$ and $\delta^{2}H_{kaol}$ measurements, resulting from somewhat poorly-constrained processes, to what extent can the calculated $\delta^{18}O_{sw}$ and $\delta^{2}H_{sw}$ agree or disagree with the relatively well-constrained physics of covariations on or below the LMWL? We implement the inverse model using datasets from two studies: Eocene high latitude Finland[21], and another from the Eocene mid-latitudes in the western United States[29].

Seasonality controls on clay fractionation lines

Figure 1 shows the simulation results from our model conceptualization (Case 1) that considers the seasonality of precipitation isotopic composition and temperature at which the clay [here using kaolinite] has formed. Case 1 presents some modifications of the status quo method concerning kaolinite lines that were used widely in previous works[18,27,48,21,29]. First, we look at the case where the waters from which the clay form fall along a defined meteoric water line (the GMWL in this case) with no evaporation (open black circles in Figure 1A). Variations parallel to clay lines of constant temperature are due to seasonal changes in meteoric waters (black circles in Figure 1B) only. Long term changes in the mean annual isotopic composition of precipitation with no change in temperature, as described by ref. 27, would also fall along arrays parallel to clay lines (Box 1). Such changes due to elevation on tectonic timescales, however, are also likely to be accompanied by changes in temperature[68].

Next, we implement covariation in the seasonality of the isotopic composition of precipitation and temperature both positively and negatively (green and orange points in Figure 1B, based on the temperature and isotope insets). Mid-latitude locations, particularly mediterranean climates, are positively correlated due to the influence of temperature on equilibrium condensation fractionation processes during precipitation. Implementing such a monthly calculation results in rotation around the mean annual temperature line where the calculated seasonal clay line is steeper than the status quo clay lines with a slope of ~12.1 (green points). Conversely, if the isotopic composition of precipitation and temperature are negatively correlated, a less likely scenario but possible to some extent in high elevation monsoon dominated regions, rotation around the status quo leads to a shallower slope of ~5.9

(orange points). Note that the precise slope of rotation in this example is dependent on the degree of seasonality in the isotopic composition of precipitation and temperature. In the below section we modify this approach by incorporating the depth dependent trends in soil pore water stable isotopes and temperature fluctuations.

Impact of soil water evaporation and soil temperature variations

Except in the case of inceptisols clay minerals typically do not form near the surface of soil and weathering profiles due to the depletion of primary minerals from which they form and instead clay mineral weathering fronts are typically found associated with weathering fronts at 10s of cm to 100s of cm depth depending on climate, lithology and soil age[69-78]. However, processes including soil pore water evaporation and temperature fluctuations likely influence the isotopic composition of clay minerals with depth near, at and below the weathering front. Our work here represents the first attempts to model the expected depth profile of the clay mineral isotopic composition accurately as a function of both processes, but does not infer at what depths clay mineral formation is occurring. Such work would require a depth-dependent reactive transport model.

Figure 1A shows the results of soil evaporation trajectories seasonally. The maximum evaporative values along monthly evaporation slopes of 3 set the $\delta^{18}O_{surface}$ and $\delta^{2}H_{surface}$ values in Equation 5 leading to an enrichment towards the surface in pore water values as shown in Figure 1C for $\delta^{18}O$. Additionally, temperature variation at the surface is set to co-vary positively with the $\delta^{18}O$ and $\delta^{2}H$ of precipitation (e.g., a mid-latitude type system), and is propagated downward as described by Equation 6 in Figure 1D. Due to the differences in fractionation factor magnitudes (kinetic evaporation slopes versus clay mineral formation temperatures) the result is that the monthly modeled $\delta^{18}O$ of kaolinite trends with depth cross (Fig. 1E), whereas the less sensitive $\delta^{2}H$ system is primarily a translation of the pore water depth trend (Fig. 1F).

Translating these calculations into monthly $\delta^{18}O_{kaolinite}$ versus $\delta^{2}H_{kaolinite}$ trajectories in comparison to the status quo thermometry clay line contours (Fig. 2G) illustrates several key potential issues with the status quo methodology. Most significantly the effect of significant evaporation away from the GMWL results in widely variable trajectories dependent on the relationship between the timing of the evaporation of soil pore waters and the timing of clay mineral formation. It is entirely possible that soil pore waters that are evaporatively enriched are those most likely to have sufficiently long residence times to carry out net weathering reactions to form clays in the soil profile[79], and thus are the most likely to be recorded. As will be discussed subsequently, such trends have been robustly observed in the geologic record[29]. However, as a counterpoint, if that is not the case and pore waters falling close to the meteoric water line are the dominant isotopic composition from which clays form, the influence of soil temperature variability in response to seasonal temperature fluctuations is non-linear and produces monthly trajectories counter (and in some cases perpendicular) to the status quo clay line thermometry contours. Such trends have also been previously observed in some Cenozoic clay isotope datasets[20,27].

Application to modern soil pore water datasets

Figure 2 shows results of the forward model, implemented at Luquillo, Puerto Rico (Fig. 2A and Fig. 2B) and Corvallis, Oregon (Fig. 2C and Fig. 2D). Average monthly precipitation

$\delta^{18}O$ and air temperature are generally negatively correlated at Luquillo (Fig. 2B inset) and positively correlated at Corvallis (Fig. 2D inset).

Using soil depth-dependent temperatures of between 25 and 26.6 °C, the forward model estimates status quo clay formation temperatures at Luquillo between 12 and 30 °C (Fig. 2A and 2B). These estimates, however, cluster around 24 °C, close to the modern mean annual temperature of ~26 °C. The estimated trendline slope of all kaolinite $\delta^{18}O$ and $\delta^{2}H$ (6.06 ±0.22 s.e.; Fig. 3B) – which accounts for modeled soil temperature gradients and evaporative isotopic enrichment – approximates the slope of the kaolinite line (6.01 ±0.23; Fig3D, dashed blue line) – which accounts for monthly seasonality in air temperature and the isotopic compositions of meteoric water. The reduction in slope reflects the slight negative covariation between monthly precipitation $\delta^{18}O$ and temperature. This suggests that, at this location where precipitation water $\delta^{18}O$ and air temperature are negatively correlated, purely atmospheric considerations (Case 1) should sufficiently describe kaolinite formation temperatures to first order. We interpret this as underlining the importance of precipitation water $\delta^{18}O$ and air temperature seasonal variability in estimating kaolinite formation temperatures. That said, sufficient data, ideally depth resolved, would be necessary to define the kaolinite trend as the most evaporatively enriched pore water data from Luquillo translate to temperatures <20 °C if taken at face value.

Using soil depth-dependent temperatures of between 8.4 and 16.4 °C down to 100 cm for the dry season, the forward model estimates status quo clay formation temperatures at Corvallis between 0 and 20 °C (Fig. 2C and 2D). These estimates, however, cluster around 10 °C, close to the modern mean annual temperature of ~9 °C. The estimated trendline slope of all kaolinite $\delta^{18}O$ and $\delta^{2}H$ (6.1 ±0.18 s.e.; Fig. 2D) – which accounts for modeled soil temperature gradients and evaporative isotopic enrichment – is shallower than the slope of the kaolinite line (11 ±1.4; Fig. 3D, dashed blue line) – which accounts for monthly air temperature and isotopic compositions of meteoric water. This suggests that, at this location where precipitation water $\delta^{18}O$ and air temperature are positively correlated with a large seasonal amplitude, purely atmospheric considerations (Case 1) will tend to underestimate kaolinite formation temperatures; whereas atmospheric and soil evaporation considerations (combined Cases 2 and 3) more closely approximate the plausible expectation that kaolinite formation temperatures derived from theses soils are likely to be warmer than the case would be in a purely atmospheric sense. Patterns of kaolinite formation temperatures are also apparent with depth following the pore water dataset, suggesting a depth-dependent decrease in temperature. That is, evaporatively enriched soils close to the surface tend to correspond to warmer clay formation temperatures, systematically from 20 cm down. There is, however, an apparent departure of kaolinite values from Case 2 that accounts for purely soil evaporation (Fig. 2D, green dashed line). This example demonstrates the importance of both soil temperature gradients, in addition to the role of precipitation water $\delta^{18}O$ and air temperature seasonal variability, in setting the isotopic composition of kaolinite and thus the inferred kaolinite formation temperatures. Additionally, it is clear from this example that pairing soil pore water and kaolinite stable isotope datasets with inferred weathering front advance depths[71,74] would provide insights into the timing (seasonality) and dominant depth(s) of clay mineral formation.

Application to paleo weathering profile datasets

Next, to illustrate the concepts developed in this paper we turn to two geologic clay stable isotope datasets from the literature. As far as we are aware, no paired soil pore water and modern clay stable isotope exists in the published literature to allow benchmarking of our model. We note that Holocene and Last Glacial Maximum soil kaolinite datasets from Colombia were previously published by ref. 17 but no accompanying soil pore water data is available. Both of the geologic datasets contain paired kaolinite hydrogen and oxygen isotope values, however, the trends relative to the GMWL are opposite, displaying steeper and shallower slopes (e.g., Fig, 1B).

In Figure 3A we plot Eocene kaolinite data from ref. 21 derived from weathering profiles in Finland[80-81]. These data come from deep weathering zones, where we anticipate minimal influence of evaporation. Surprisingly the $\delta^{18}O$-$\delta^{2}H$ array of the kaolinite data appears nearly vertical. Applying the approach outlined in Figure 1B and increasing the formation temperatures and isotopic compositions seasonally form a clay array with a slope of ~31. To derive a parsimonious explanation for the vertical nature of the data in equilibrium with the modern local meteoric water requires a uniform shift in the temperature seasonality to ~8 °C warmer on average. The inference of warmer temperatures was made by ref. 21, but the kaolinite array slope >8 was not described. Isotope-enabled global climate model simulations suggest that while a compressed GMWL would have been present in the Eocene the slope and intercept of the GMWL would have been similar to today[82]. As such, the counterclockwise rotation about the GMWL observed in the Finland kaolinites suggests: 1) no role for evaporation in a deep weathering zone, 2) positive covariation in the seasonality of temperature and $\delta^{18}O$-$\delta^{2}H$ variations, and 3) formation temperature ~8 °C warmer than modern, though as we illustrate in the example from Corvallis above, interpreting such data with respect to paleotemperatures requires a nuanced approach.

The second contrasting example is from weathered Eocene river sediments from the west flank of the northern Sierra Nevadas[29,83-86]. The $\delta^{2}H$ of the kaolinites were originally published by Mulch et al. (2006) to illustrate relatively high Eocene elevations, which were also confirmed by $\delta^{2}H$ analyses of volcanic glass and organic biomarkers[87,88]. Subsequently, ref. 29 paired the kaolinite $\delta^{2}H$ measurements on the same samples used by ref. 83 and found a shallower inferred $\delta^{18}O$ gradient and an apparent $\delta^{18}O$-$\delta^{2}H$ trend that reflected evaporation in the weathering zone with a slope of ~2.3 across the entire dataset (Fig, 3B). This finding is not surprising given that these Eocene river gravels represent immature weathering profiles; however, waters along the windward side of a mountain range such as the Eocene Sierra Nevada should fall along a meteoric water line similar to today (slope of ~7.3)[89]. As such, in Figure 3B we apply our methodology here to explain how previous estimates by ref. 29 likely used source water values too enriched than the local meteoric values causing an underestimate in past elevation. To do so requires assuming a warmer temperature of formation, ~33 °C than previously estimated 23.2±6.4 °C[29] and correcting the calculated pore water values along the inferred evaporation slope (~2.3). This assumes a summertime Eocene formation temperature and a strongly evaporative system (although actual sampling depths in the various weathering profiles were not quantified). Doing so places the most depleted samples near the modern local meteoric water line and calculation of source waters are presented in histograms in Figure 3. This set of calculations demonstrates that with some assumptions, such as warmer (likely

summertime) formation temperatures during the Eocene hothouse and maximally evaporative soil pore water conditions, applying our inverse model approach better aligns the previously published clay $\delta^{18}O$-$\delta^{2}H$ stable isotope data with the volcanic glass and organic biomarker paleoelevation estimates (cf. ref. 90).

Outlook and Conclusions

The framework developed here extends the utility of paired clay $\delta^{18}O$ and $\delta^{2}H$ datasets from geologic and modern weathering profiles. While the factors described here necessarily complicate the use of $\delta^{18}O$ and $\delta^{2}H$ measurements as a single mineral thermometer, the work here outlines the approaches needed to develop a robust 'proxy system model'[59,91-93] for geologic use and demonstrates how such measurements on modern weathering profiles, which are currently limited, may provide important insights into weathering profile development and clay formation processes. Additionally, further work pairing the modeling developed here to a reactive transport weathering framework for primary mineral dissolution, clay mineral formation and weathering front advance[71,74,78] will be necessary to fully describe the system.

To conclude, the work here demonstrated the effect of three processes previously not considered but widely observed in modern systems: 1) surface temperature seasonality and covariation of temperature with meteoric water $\delta^{18}O$-$\delta^{2}H$ variations, 2) soil pore water evaporation, and 3) soil temperature variations with depth. We demonstrated using both a forward model of modern soil pore waters and an inverse model of geologic data how all three processes may play a role in the interpretation and utility of clay $\delta^{18}O$ and $\delta^{2}H$ datasets. While these effects have been discussed qualitatively or schematically/graphically in previous work[27,94], this work provides the first modeling framework to refine this methodology based on modern and paleo observations across a diversity of climatological locations and pedogenic settings where clays are formed.

References

1. Urey, H. C. The thermodynamic properties of isotopic substances. J. Chem. Soc. 562–581 (1947).

2. Dansgaard, W. Stable Isotopes in Precipitation. Tellus 16, 436–468 (1964).

3. Gat, J. R. Oxygen and hydrogen isotopes in the hydrologic cycle. Annu. Rev. Earth Planet. Sci. 24, 225–262 (1996).

4. Aggarwal, P. K., Gat, J. R. & Froehlich, K. F. O. Isotopes in the water cycle: Past, present and future of a developing science. Isot. Water Cycle Past, Present Futur. a Dev. Sci. 1–381 (2005) doi:10.1007/1-4020-3023-1/COVER.

5. Bowen, G. J., Cai, Z., Fiorella, R. P. & Putman, A. L. Isotopes in the Water Cycle: Regional- to Global-Scale Patterns and Applications. Annu. Rev. Earth Planet. Sci. 47, 453–479 (2019).

6. Craig, H. Isotopic variations in meteoric waters. Science (80-.). 133, 1702–1703 (1961).

7. Craig, H., Gordon L.I. Deuterium and oxygen-18 variations in the ocean and the marine atmosphere. In E Tongiorgi, ed, Proceedings of a Conference on Stable Isotopes in Oceanographic Studies and Paleotemperatures. Spoleto, Italy, pp 9–130 (1965).

8. Gonfiantini, R. Environmental isotopes in lake studies. Handb. Environ. Isot. Geochemistry (1986).

9. Gonfiantini, R., Wassenaar, L. I., Araguas-Araguas, L. & Aggarwal, P. K. A unified Craig-Gordon isotope model of stable hydrogen and oxygen isotope fractionation during fresh or saltwater evaporation. Geochim. Cosmochim. Acta 235, 224–236 (2018).

10. Aron, P. G. et al. Triple oxygen isotopes in the water cycle. Chem. Geol. 565, 120026 (2021).

11. O'Neil, J. R., Clayton, R. N. & Mayeda, T. K. Oxygen Isotope Fractionation in Divalent Metal Carbonates. J. Chem. Phys. 51, 5547–5558 (2003).

12. Capuano, R. M. The temperature dependence of hydrogen isotope fractionation between clay minerals and water: Evidence from a geopressured system. Geochim. Cosmochim. Acta 56, 2547–2554 (1992).

13. Kim, S. T. & O'Neil, J. R. Equilibrium and nonequilibrium oxygen isotope effects in synthetic carbonates. Geochim. Cosmochim. Acta 61, 3461–3475 (1997).

14. Savin, S. M. & Epstein, S. The oxygen and hydrogen isotope geochemistry of clay minerals. Geochim. Cosmochim. Acta 34, 25–42 (1970).

15. O'Neil, J. R. & Kharaka, Y. K. Hydrogen and oxygen isotope exchange reactions between clay minerals and water. Geochim. Cosmochim. Acta 40, 241–246 (1976).

16. Gilg, H. A. D–H evidence for the timing of kaolinization in Northeast Bavaria, Germany. Chem. Geol. 170, 5–18 (2000).

17. Mora, G. & Pratt, L. M. Isotopic evidence for cooler and drier conditions in the tropical Andes during the last glacial stage. Geology 29, 519–522 (2001).

18. Vitali, F., Longstaffe, F. J., McCarthy, P. J., Plint, A. G. & Caldwell, W. G. E. Stable isotopic investigation of clay minerals and pedogenesis in an interfluve paleosol from the Cenomanian Dunvegan Formation, N.E. British Columbia, Canada. Chem. Geol. 192, 269–287 (2002).

19. Gilg, H. A. et al. Genesis of amethyst geodes in basaltic rocks of the Serra Geral Formation (Ametista do Sul, Rio Grande do Sul, Brazil): a fluid inclusion, REE, oxygen, carbon, and Sr isotope study on basalt, quartz, and calcite. Miner. Depos. 38, 1009–1025 (2003).

20. Sjostrom, D. J., Hren, M. T., Horton, T. W., Waldbauer, J. R. & Chamberlain, C. P. Stable isotopic evidence for a pre–late Miocene elevation gradient in the Great Plains–Rocky Mountain region, USA. in Tectonics, Climate, and Landscape Evolution (eds. Willett, S. D., Hovius, N., Brandon, M. T. & Fisher, D. M.) vol. 398 0 (Geological Society of America, 2006).

21. Gilg, H. A., Hall, A. M., Ebert, K. & Fallick, A. E. Cool kaolins in Finland. Palaeogeogr. Palaeoclimatol. Palaeoecol. 392, 454–462 (2013).

22. Tabor, N. J. & Montañez, I. P. Oxygen and hydrogen isotope compositions of Permian pedogenic phyllosilicates: Development of modern surface domain arrays and implications for paleotemperature reconstructions. Palaeogeogr. Palaeoclimatol. Palaeoecol. 223, 127–146 (2005).

23. Feng, W. & Yapp, C. J. 18O/16O and D/H ratios of pedogenic kaolinite in a North American Cenomanian laterite: Paleoclimatic implications. Geochim. Cosmochim. Acta 73, 6249–6263 (2009).

24. Muttik, N., Kirsimäe, K. & Vennemann, T. W. Stable isotope composition of smectite in suevites at the Ries crater, Germany: Implications for hydrous alteration of impactites. Earth Planet. Sci. Lett. 299, 190–195 (2010).

25. Meyer, I., Davies, G. R. & Stuut, J.-B. W. Grain size control on Sr-Nd isotope provenance studies and impact on paleoclimate reconstructions: An example from deep-sea sediments offshore NW Africa. Geochemistry, Geophys. Geosystems 12, (2011).

26. Rosenau, N. A. & Tabor, N. J. Oxygen and hydrogen isotope compositions of paleosol phyllosilicates: Differential burial histories and determination of Middle–Late Pennsylvanian low-latitude terrestrial paleotemperatures. Palaeogeogr. Palaeoclimatol. Palaeoecol. 392, 382–397 (2013).

27. Mix, H. T. & Chamberlain, C. P. Stable isotope records of hydrologic change and paleotemperature from smectite in Cenozoic western North America. Geochim. Cosmochim. Acta 141, 532–546 (2014).

28. Hall, A. M., Gilg, H. A., Fallick, A. E. & Merritt, J. W. Kaolins in gravels and saprolites in north-east Scotland: Evidence from stable H and O isotopes for Palaeocene–Miocene deep weathering. Palaeogeogr. Palaeoclimatol. Palaeoecol. 424, 6–16 (2015).

29. Mix, H. T., Ibarra, D. E., Mulch, A., Graham, S. A. & Chamberlain, C. P. A hot and high Eocene Sierra Nevada. GSA Bull. 128, 531–542 (2016).

30. Gao, Z., Weng, H. & Guo, H. Unraveling influences of nitrogen cycling on arsenic enrichment in groundwater from the Hetao Basin using geochemical and multi-isotopic approaches. J. Hydrol. 595, 125981 (2021).

31. Stern, L. A., Chamberlain, C. P., Reynolds, R. C. & Johnson, G. D. Oxygen isotope evidence of climate change from pedogenic clay minerals in the Himalayan molasse. Geochim. Cosmochim. Acta 61, 731–744 (1997).

32. Tabor, N. J., Montanez, I. P. & Southard, R. J. Paleoenvironmental reconstruction from chemical and isotopic compositions of Permo-Pennsylvanian pedogenic minerals. Geochim. Cosmochim. Acta 66, 3093–3107 (2002).

33. John, S. G., Mendez, J., Moffett, J. & Adkins, J. The flux of iron and iron isotopes from San Pedro Basin sediments. Geochim. Cosmochim. Acta 93, 14–29 (2012).

34. Kukla, T. et al. High-Resolution Stable Isotope Paleotopography of the John Day Region, Oregon, United States . Frontiers in Earth Science vol. 9 at https://www.frontiersin.org/articles/10.3389/feart.2021.635181 (2021).

35. Knauth, L. P. & Epstein, S. Hydrogen and oxygen isotope ratios in nodular and bedded cherts. Geochim. Cosmochim. Acta 40, 1095–1108 (1976).

36. Kolodny, Y. & Epstein, S. Stable isotope geochemistry of deep sea cherts. Geochim. Cosmochim. Acta 40, 1195–1209 (1976).

37. Abruzzese, M. J., Waldbauer, J. R. & Chamberlain, C. P. Oxygen and hydrogen isotope ratios in freshwater chert as indicators of ancient climate and hydrologic regime. Geochim. Cosmochim. Acta 69, 1377–1390 (2005).

38. Ibarra, D. E., Kukla, T., Methner, K. A., Mulch, A. & Chamberlain, C. P. Reconstructing Past Elevations From Triple Oxygen Isotopes of Lacustrine Chert: Application to the Eocene Nevadaplano, Elko Basin, Nevada, United States . Frontiers in Earth Science vol. 9 at https://www.frontiersin.org/articles/10.3389/feart.2021.628868 (2021).

39. Yapp, C. J. Oxygen and hydrogen isotope variations among goethites (α-FeOOH) and the determination of paleotemperatures. Geochim. Cosmochim. Acta 51, 355–364 (1987).

40. Yapp, C. J. Oxygen isotope effects associated with the solid-state α-FeOOH to α-Fe2O3 phase transformation. Geochim. Cosmochim. Acta 54, 229–236 (1990).

41. Tabor, N. J., Yapp, C. J. & Montanez, I. P. Goethite, calcite, and organic matter from Permian and Triassic soils: carbon isotopes and CO2 concentrations. Geochim. Cosmochim. Acta 68, 1503–1517 (2004).

42. Amin, A. et al. Depth distribution of soil water sourced by plants at the global scale: A new direct inference approach. Ecohydrology 13, e2177 (2020).

43. Sprenger, M. et al. Storage, mixing, and fluxes of water in the critical zone across northern environments inferred by stable isotopes of soil water. Hydrol. Process. 32, 1720–1737 (2018).

44. Benettin, P. et al. Effects of climatic seasonality on the isotopic composition of evaporating soil waters. Hydrol. Earth Syst. Sci. 22, 2881–2890 (2018).

45. Bowen, G. J. et al. Inferring the source of evaporated waters using stable H and O isotopes. Oecologia 187, 1025–1039 (2018).

46. Knighton, J., Singh, K. & Evaristo, J. Understanding Catchment-Scale Forest Root Water Uptake Strategies Across the Continental United States Through Inverse Ecohydrological Modeling. Geophys. Res. Lett. 47, (2020).

47. Delgado, A. & Reyes, E. Oxygen and hydrogen isotope compositions in clay minerals: A potential single-mineral geothermometer. Geochim. Cosmochim. Acta 60, 4285–4289 (1996).

48. Sheppard, S. M. F. & Gilg, H. A. Stable isotope geochemistry of clay minerals: “The story of sloppy, sticky, lumpy and tough” Cairns-Smith (1971). Clay Miner. 31, 1–24 (1996).

49. Savin, S. M. & Hsieh, J. C. C. The hydrogen and oxygen isotope geochemistry of pedogenic clay minerals: principles and theoretical background. Geoderma 82, 227–253 (1998).

50. Bird, M. I., Longstaffe, F. J., Fyfe, W. S. & Bildgen, P. Oxygen-isotope systematics in a multiphase weathering system in Haiti. Geochim. Cosmochim. Acta 56, 2831–2838 (1992).

51. Bird, M. I. & Chivas, A. R. Geomorphic and palaeoclimatic implications of an oxygen-isotope chronology for Australian deeply weathered profiles. Aust. J. Earth Sci. 40, 345–358 (1993).

52. Dee, S. G., Bailey, A., Conroy, J. L., Atwood, A., Stevenson, S., Nusbaumer, J., & Noone, D. Water isotopes, climate variability, and the hydrological cycle: recent advances and new frontiers. Environmental Research: Climate (2023). doi: 10.1088/2752-5295/accbe1

53. Rozanski, K., Araguás-Araguás, L. & Gonfiantini, R. Isotopic Patterns in Modern Global Precipitation. in Climate Change in Continental Isotopic Records 1–36 (1993). doi: 10.1029/GM078p0001.

54. Dawson, T. E. & Simonin, K. A. The Roles of Stable Isotopes in Forest Hydrology and Biogeochemistry BT - Forest Hydrology and Biogeochemistry: Synthesis of Past Research and Future Directions. in (eds. Levia, D. F., Carlyle-Moses, D. & Tanaka, T.) 137–161 (Springer Netherlands, 2011). doi:10.1007/978-94-007-1363-5_7.

55. Gibson, J. J., Birks, S. J. & Edwards, T. W. D. Global prediction of δA and δ2H-δ18O evaporation slopes for lakes and soil water accounting for seasonality. Global Biogeochem. Cycles 22, (2008).

595 56. Zimmermann, U., MüNnich, K. O. & Roether, W. Downward Movement of Soil Moisture
596 Traced by Means of Hydrogen Isotopes. in Isotope Techniques in the Hydrologic Cycle 28–
597 36 (1967). doi:https://doi.org/10.1029/GM011p0028.

598 57. Chamberlain, C. P., Winnick, M. J., Mix, H. T., Chamberlain, S. D. & Maher, K. The
599 impact of neogene grassland expansion and aridification on the isotopic composition of
600 continental precipitation. Global Biogeochem. Cycles 28, 992–1004 (2014).

601 58. Barnes, C. J. & Allison, G. B. The distribution of deuterium and 18O in dry soils: 1.
602 Theory. J. Hydrol. 60, 141–156 (1983).

603 59. Fischer-Femal, B. J. & Bowen, G. J. Coupled carbon and oxygen isotope model for
604 pedogenic carbonates. Geochim. Cosmochim. Acta 294, 126–144 (2021).

605 60. Passey, B. H., Levin, N. E., Cerling, T. E., Brown, F. H. & Eiler, J. M. High-temperature
606 environments of human evolution in East Africa based on bond ordering in paleosol
607 carbonates. Proc. Natl. Acad. Sci. 107, 11245–11249 (2010).

608 61. Quade, J., Eiler, J., Daëron, M. & Achyuthan, H. The clumped isotope geothermometer
609 in soil and paleosol carbonate. Geochim. Cosmochim. Acta 105, 92–107 (2013).

610 62. Gallagher, T. M., Cacciatore, C. G. & Breecker, D. O. Interpreting the Difference in
611 Magnitudes of PETM Carbon Isotope Excursions in Paleosol Carbonate and Organic Matter:
612 Oxidation of Methane in Soils Versus Elevated Soil Respiration Rates. Paleoceanogr.
613 Paleoclimatology 34, 2113–2128 (2019).

614 63. Kelson, J. R. et al. A proxy for all seasons? A synthesis of clumped isotope data from
615 Holocene soil carbonates. Quat. Sci. Rev. 234, 106259 (2020).

616 64. Hillel, D. in Introduction to Soil Physics (Hillel, D.) 155-172 (Academic Press, 1982).

617 65. Savin, S. M. & Lee, M. Isotopic studies of phyllosilicates. Rev. Mineral. Geochemistry 19,
618 189–223 (1988).

619 66. Evaristo, J., McDonnell, J. J., Scholl, M. A., Bruijnzeel, L. A. & Chun, K. P. Insights into
620 plant water uptake from xylem-water isotope measurements in two tropical catchments with
621 contrasting moisture conditions. Hydrol. Process. n/a-n/a (2016) doi:10.1002/hyp.10841.

622 67. Renée Brooks, J., Barnard, H. R., Coulombe, R. & McDonnell, J. J. Ecohydrologic
623 separation of water between trees and streams in a Mediterranean climate. Nat. Geosci. 3,
624 100–104 (2010).

625 68. Heitmann, E. O., Hyland, E. G., Schoettle-Greene, P., Brigham, C. A. P. & Huntington,
626 K. W. Rise of the Colorado Plateau: A Synthesis of Paleoelevation Constraints From the
627 Region and a Path Forward Using Temperature-Based Elevation Proxies . Frontiers in

628 Earth Science vol. 9 at https://www.frontiersin.org/articles/10.3389/feart.2021.648605
629 (2021).

630 69. Chamberlain, C. P., Waldbauer, J. R., & Jacobson, A. D. Strontium, hydrothermal
631 systems and steady-state chemical weathering in active mountain belts. Earth and Planetary
632 Science Letters, 238(3-4), 351-366 (2005).

633 70. Ferrier, K. L. & Kirchner, J. W. Effects of physical erosion on chemical denudation rates:
634 A numerical modeling study of soil-mantled hillslopes. Earth Planet. Sci. Lett. 272, 591–599
635 (2008).

636 71. Brantley, S. L., White, A. F. & Kubicki, J. D. Kinetics of water-rock interaction. Kinet.
637 Water-Rock Interact. 1–833 (2008) doi:10.1007/978-0-387-73563-4/COVER.

638 72. White, A. F., et al. Chemical weathering of a marine terrace chronosequence, Santa
639 Cruz, California I: interpreting rates and controls based on soil concentration–depth profiles.
640 Geochimica et Cosmochimica Acta, 72(1), 36-68 (2008).

641 73. White, A. F. et al. Chemical weathering of a marine terrace chronosequence, Santa
642 Cruz, California. Part II: Solute profiles, gradients and the comparisons of contemporary and
643 long-term weathering rates. Geochimica et Cosmochimica Acta, 73(10), 2769-2803 (2009).

644 74. Maher, K., Steefel, C. I., White, A. F. & Stonestrom, D. A. The role of reaction affinity and
645 secondary minerals in regulating chemical weathering rates at the Santa Cruz Soil
646 Chronosequence, California. Geochim. Cosmochim. Acta 73, 2804–2831 (2009).

647 75. Hewawasam, T. et al. Slow advance of the weathering front during deep, supply-limited
648 saprolite formation in the tropical Highlands of Sri Lanka. Geochim. Cosmochim. Acta 118,
649 202–230 (2013).

650 76. Druhan, J. L. & Maher, K. A Model Linking Stable Isotope Fractionation to Water Flux
651 and Transit Times in Heterogeneous Porous Media. Procedia Earth Planet. Sci. 10, 179–
652 188 (2014).

653 77. Behrens, R., Bouchez, J., Schuessler, J. A., Dultz, S., Hewawasam, T., & von
654 Blanckenburg, F. Mineralogical transformations set slow weathering rates in low-porosity
655 metamorphic bedrock on mountain slopes in a tropical climate. Chemical Geology, 411,
656 283-298 (2015).

657 78. Winnick, M. J., Druhan, J. L., & Maher, K. (2022). Weathering intensity and lithium
658 isotopes: A reactive transport perspective. American Journal of Science, 322(5), 647-682.

659 79. Maher, K. The dependence of chemical weathering rates on fluid residence time. Earth
660 Planet. Sci. Lett. 294, 101–110 (2010).

80. T. Al-Ani, O. Sarapää, & M.J. Lehtinen, Mineralogical and chemical study of some kaolin samples from the Kahdeksaisiensuo and Hyväjärvi occurrences, Virtasalmi, SE Finland, Geological Survey of Finland, Report M19/3232/2006/1/822010, Espoo (2006), p. 19

81. P. Lintinen, Kaoliinitutkimukset Sodankylän Kelujärven ympäristössä 2003–2004, Geological Survey of Finland, Report M19/3713,3714,3731,3732/2006/1/82, Espoo (2006), p. 7

82. Speelman, E. N. et al. Modeling the influence of a reduced equator-to-pole sea surface temperature gradient on the distribution of water isotopes in the Early/Middle Eocene. Earth Planet. Sci. Lett. 298, 57–65 (2010).

83. Mulch, A., Graham, S. A. & Chamberlain, C. P. Hydrogen Isotopes in Eocene River Gravels and Paleoelevation of the Sierra Nevada. Science (80-.). 313, 87–89 (2006).

84. Cassel, E. J. & Graham, S. A. Paleovalley morphology and fluvial system evolution of Eocene–Oligocene sediments (“auriferous gravels”), northern Sierra Nevada, California: Implications for climate, tectonics, and topography. GSA Bull. 123, 1699–1719 (2011).

85. Henry, C. D. et al. Eocene–Early Miocene paleotopography of the Sierra Nevada–Great Basin–Nevadaplano based on widespread ash-flow tuffs and paleovalleys. Geosphere 8, 1–27 (2012).

86. Cassel, E. J., Breecker, D. O., Henry, C. D., Larson, T. E. & Stockli, D. F. Profile of a paleo-orogen: High topography across the present-day Basin and Range from 40 to 23 Ma. Geology 42, 1007–1010 (2014).

87. Cassel, E. J., Graham, S. A. & Chamberlain, C. P. Cenozoic tectonic and topographic evolution of the northern Sierra Nevada, California, through stable isotope paleoaltimetry in volcanic glass. Geology 37, 547–550 (2009).

88. Hren, M. T., Pagani, M., Erwin, D. M. & Brandon, M. Biomarker reconstruction of the early Eocene paleotopography and paleoclimate of the northern Sierra Nevada. Geology 38, 7–10 (2010).

89. Ingraham, N. L. & Taylor, B. E. Light stable isotope systematics of large-scale hydrologic regimes in California and Nevada. Water Resour. Res. 27, 77–90 (1991).

90. Mulch, A. Stable isotope paleoaltimetry and the evolution of landscapes and life. Earth Planet. Sci. Lett. 433, 180–191 (2016).

91. Evans, M. N., Tolwinski-Ward, S. E., Thompson, D. M., & Anchukaitis, K. J. Applications of proxy system modeling in high resolution paleoclimatology. Quaternary science reviews, 76, 16-28 (2013).

92. Dee, S. G., Russell, J. M., Morrill, C., Chen, Z. & Neary, A. PRYSM v2.0: A Proxy System Model for Lacustrine Archives. Paleoceanogr. Paleoclimatology 33, 1250–1269 (2018).

93. Bowen, G. J., Fischer-Femal, B., Reichart, G.-J., Sluijs, A. & Lear, C. H. Joint inversion of proxy system models to reconstruct paleoenvironmental time series from heterogeneous data. Clim. Past 16, 65–78 (2020).

94. Grujic, D. et al. Formation of a Rain Shadow: O and H Stable Isotope Records in Authigenic Clays From the Siwalik Group in Eastern Bhutan. Geochemistry, Geophys. Geosystems 19, 3430–3447 (2018).

95. Scatena, F., LCZO Meteorology, Air Temperature-Daily-Luquillo Mountains-(2002-2009), HydroShare https://www.hydroshare.org/resource/b39a41c1db56412cb3ccd3a0c042f1ec/ (2020).

96. Gregory, S.; Johnson, S. Stream and air temperature data from stream gages and stream confluences in the Andrews Experimental Forest, 1950 to present. https://doi.org/10.6073/pasta/9437d1603044f5b92189110dd8343763 (2019).

97. U.S. Geological Survey Open-File Report 2014–1101, http://dx.doi.org/10.3133/ofr20141101

98. Segura, C. Water stable isotopes for streams and precipitation samples in the HJ Andrews Experimental Forest and Mary's River Watershed, 2014-2018. Long-Term Ecological Research. Forest Science Data Bank, Corvallis, OR. https://doi.org/10.6073/pasta/00a943113f6915fab65db3979205f5f9 (2022).

99. Sodankyla Climate. Climate Data. https://en.climate-data.org/europe/finland/sodankylae/sodankylae-9794/ (2023).

100. UCANR-IPM. https://ipm.ucanr.edu/calludt.cgi/WXSTATIONDATA?STN=AUBURN.C (2023)

101. IAEA. https://websso.iaea.org/ Finland: GNIP, Finland Rovaniemi station (2023).

102. OIPC Waterisotopes.org. https://wateriso.utah.edu/waterisotopes/pages/data_access/oipc.html (2023).

103. Sheppard, S. M. F. & Gilg, H. A. Stable isotope geochemistry of clay minerals: “The story of sloppy, sticky, lumpy and tough” Cairns-Smith (1971). *Clay Miner.* **31**, 1–24 (1996).

Acknowledgements

Ibarra acknowledges Page Chamberlain, Matthew Winnick, Jeremy Caves Rugenstein, Tyler Kukla and Kate Maher for discussions on this topic that informed this work.

Author contributions

Both authors conceived of this work jointly, created the figures and wrote the manuscript.

Competing interests

The authors declare no competing interests.

Figures and Figure Captions

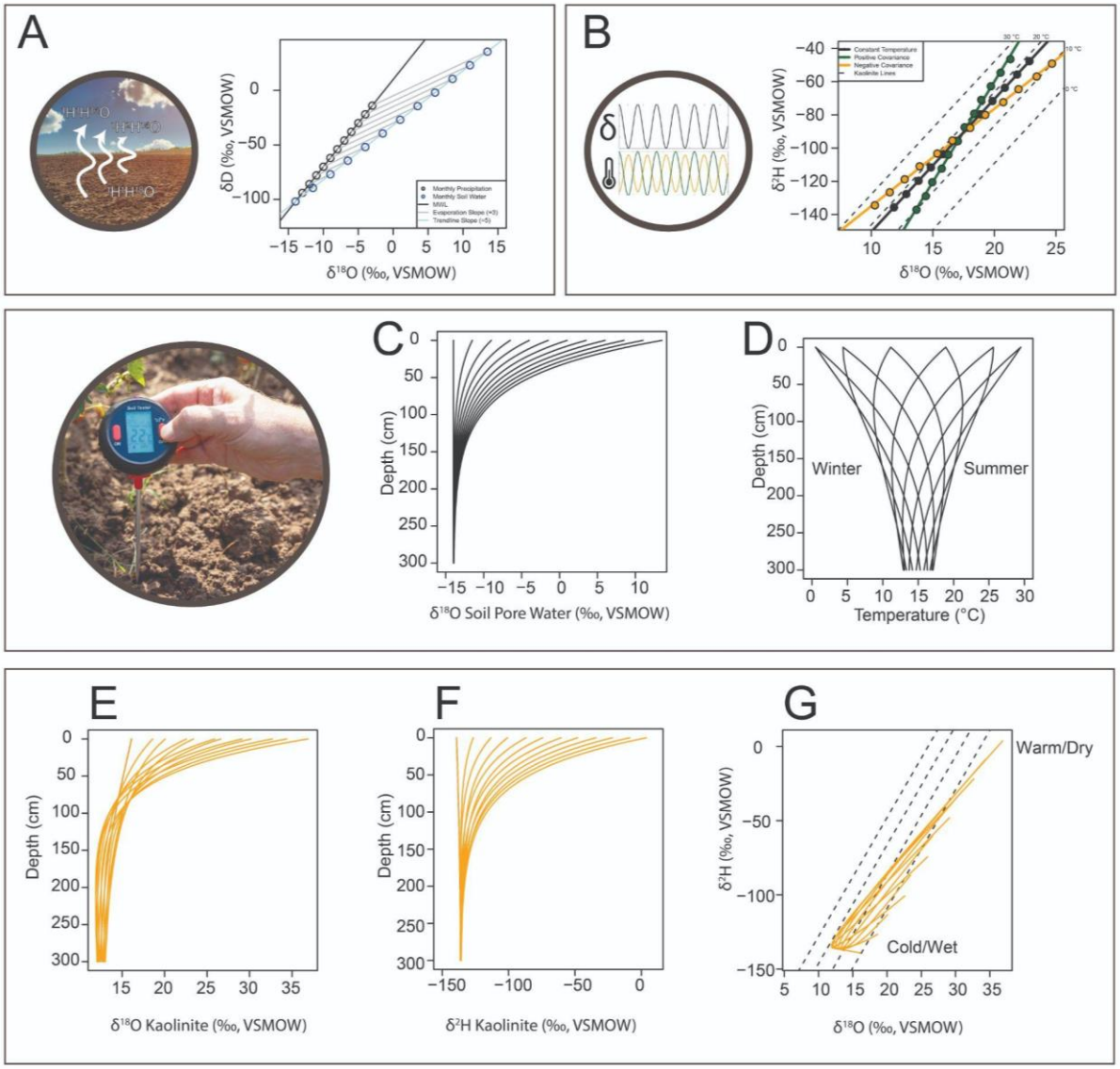

Figure 1. Conceptual framework for projection and interpretation of clay stable isotope data. **A)** Global meteoric water line (MWL) with monthly precipitation values (blackcircles) falling along the meteoric water and monthly evaporation slopes of 3 (gray line) intercepting an empirical slope of 5 (blue circles, light blue line). **B)** Impact of seasonal temperature variations on waters falling along the MWL in A) for constant temperature, positive covariance and negative covariance between the isotopic composition of water and assumed fractionation temperatures. Inset is the assumed MWL seasonal variation and hypothetical temperature variations used in B). **C)** Monthly soil pore water oxygen isotopic composition as a function of depth (Equation 5). **D)** Monthly propagation of seasonal temperature fluctuations with depth in a soil profile (Equation 6). **E)** Calculated monthly kaolinite $\delta^{18}O$ in equilibrium with soil pore water and

monthly temperature depth trends. **F)** As in E) for kaolinite δ^2H. **G)** Cross plot of monthly kaolinite $\delta^{18}O$-δ^2H (E and F) overlaid on status quo kaolinite lines (as in Box 1).

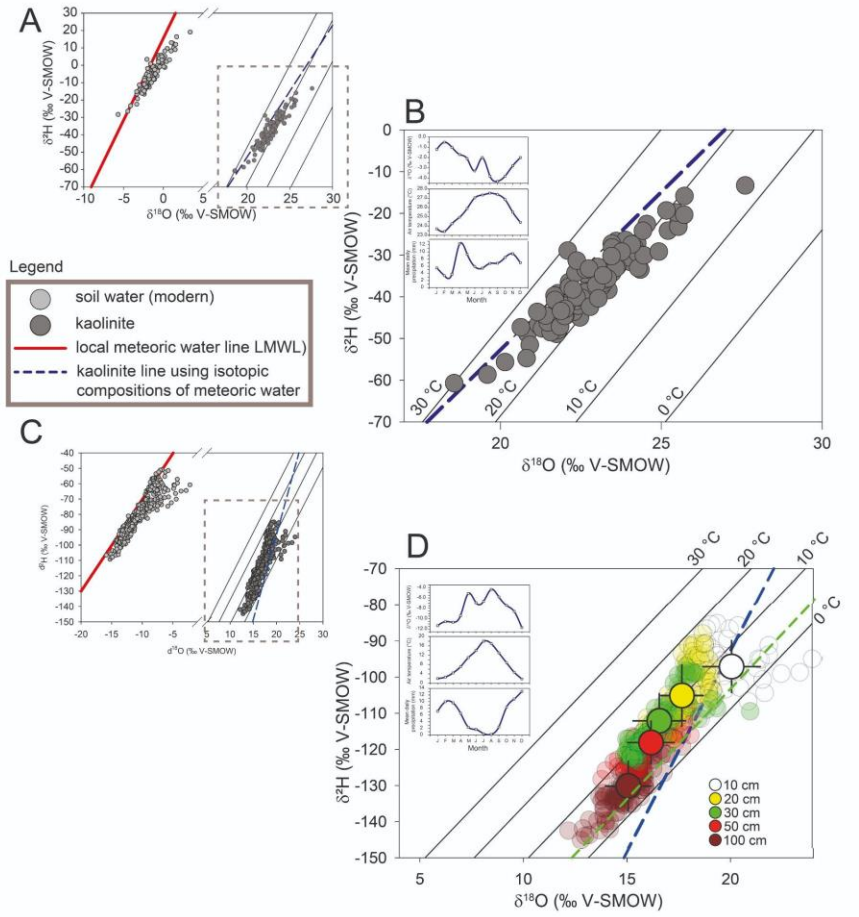

Figure 2. $\delta^{18}O$-δ^2H crossplots showing the application of the forward model to two modern soil water profiles. A) Modern soil water (filled light gray circles) and calculated kaolinite (filled dark gray circles) isotopic compositions in Luquillo, Puerto Rico (data from ref. 66). The solid red line represents the local meteoric water line (LMWL). The dashed blue line represents a regression through calculated kaolinite isotopic compositions, informed by monthly variability in air temperature and precipitation $\delta^{18}O$ and δ^2H. **B)** Magnified view of the dashed polygon in A, showing the kaolinite formation temperatures 0°C, 10°C, 20°C, and 30°C; inset shows mean monthly values of precipitation $\delta^{18}O$ (top), air temperature (middle), and daily precipitation (bottom). **C)** As in A for Corvallis, Oregon (data from ref. 67). **D)** As in B; calculated kaolinite isotopic compositions are presented per soil depth; larger circles and error bars represent mean and 1$\boldsymbol{\sigma}$, respectively; raw values are also shown in corresponding soil depth colors, in reduced transparency for visualization. The dashed green line represents a regression through calculated kaolinite isotopic compositions, informed by monthly variability in soil depth-dependent temperature (as in Figure 1G) and constrained by evaporation line slope (3.4) and maximum isotopic compositions of residual soil water derived from the Craig-Gordon model (using the algorithm of ref. 44).

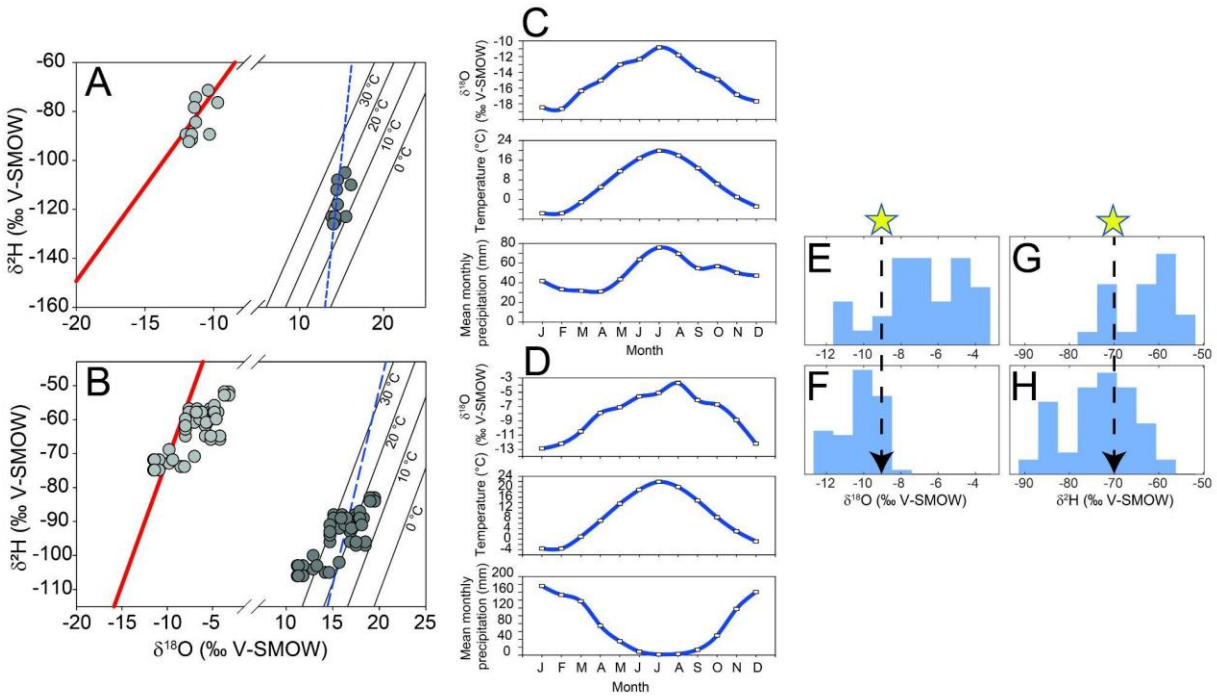

Figure 3. $\delta^{18}O$-$\delta^{2}H$ crossplots showing the application of the inverse model to two paleo soils. A) Calculated modern soil water (filled light gray circles) and measured kaolinite (filled dark gray circles) isotopic compositions in Finland (data from ref. 21). The solid red line represents the local meteoric water line (LMWL). The dashed blue line represents a regression through measured kaolinite isotopic compositions. **B)** As in A for sites in the Sierras (data from ref. 29). Also shown in A and are the kaolinite formation temperatures 0°C, 10°C, 20°C, and 30°C. **C)** Mean monthly values of precipitation $\delta^{18}O$ (top), air temperature (middle), and monthly precipitation (bottom) for the Finland sites. **D)** As in C for sites in the Sierras. **E)** Histogram of calculated soil water $\delta^{18}O$. **F)** Histogram of calculated precipitation source water $\delta^{18}O$ of E. **G)** Histogram of calculated soil water $\delta^{2}H$. **H)** Histogram of calculated precipitation source water $\delta^{2}H$ of G. Values calculated in F and H are constrained by the soil evaporation line slope (here set at 3) and tracing the source water isotopic composition as the intersection between the soil evaporation line and the LMWL. The star symbols and dashed lines represent the isotopic compositions of precipitation source waters using the approach of simply running a trendline across all soil water data demonstrating an overestimate, particularly with respect to $\delta^{18}O$.

Supplementary Information for
"Soil pore water evaporation and temperature influences on clay mineral paleothermometry"

Daniel E.Ibarra[1,2] and Jaivime Evaristo[3]

1. Institute at Brown for Environment and Society, Brown University, Providence, RI, 02906 USA
2. Department of Earth, Environmental and Planetary Science, Brown University, Providence, RI, 02906 USA
3. Copernicus Institute of Sustainable Development, Utrecht University, Utrecht, The Netherlands

This Supplementary Information (S.I.) presented below elaborates further on the rationale and methodology that underpin the study as well as providing associated caveats and limitations where further model development may be necessary. We first provide a derivation of the status quo equations, demonstrate the effect of the fractionation factor approximation that is commonly used, describe caveats and limitations of the three cases presented in the main text, and elaborate on assumptions made in the forward and inverse modeling approaches used as examples in this work. R code to implement the thought experiments and calculations in Box 1, Figure S1, S2 and S3, and MATLAB to implement the forward and inverse model calculations are provided as supplementary files.

Extended Methods

I. Derivation of status quo paleothermometry equations

While previous work has presented abbreviated derivations of the clay mineral thermometers based on hydrogen and oxygen isotopes[14, 22, 26, 27, 29, 47] the mathematical operations required to go from two fractionation factor equations and the meteoric water line (equations 1 and 2) to the single mineral thermometry equations (equations 3 and 4) are not formally derived in the peer review literature. For completeness we do so here using kaolinite as the example mineral. Starting from the kaolinite fractionation factors from ref. 48 for oxygen:

$$1000 \times \ln\alpha_{kaol\text{-}water\text{-}O} = 2.76\times10^{6} \times T^{-2} - 6.75 \quad \text{(S1)}$$

and for hydrogen:

$$1000 \times \ln\alpha_{kaol\text{-}water\text{-}H} = -2.2\times10^{6} \times T^{-2} - 7.7 \quad \text{(S2).}$$

Then taking the global meteoric water line as our third constraint:

$$\delta^{2}H = 8\times\delta^{18}O + 10 \quad \text{(S3),}$$

and the approximation for $1000\ln\alpha$ (see next section) as the difference between two phases, we are left with the following two equations:

$$\delta^{18}O_{kaol} - \delta^{18}O_{sw} = 2.76x10^{6} \times T^{-2} - 6.75 \quad \text{(S4)}$$

and

$$\delta^{2}H_{kaol} - \delta^{2}H_{sw} = -2.2x10^{6} \times T^{-2} - 7.7 \quad \text{(S5).}$$

Assuming waters fall along the meteoric water line (a key assumption questioned by this work), and plugging equations 4 and 5 into the GMWL, equation 3, gives the following expanded equation:

$$\delta^{2}H_{kaol} + 2.2x10^{6} \times T^{-2} - 7.7 = 8*(\delta^{18}O_{kaol} - 2.76x10^{6} \times T^{-2} - 6.75) + 10 \quad \text{(S6).}$$

Rearranging for $10^{6} \times T^{-2}$ and simplifying terms leads to equation 3 from the main text:

$$3.0350 \times 10^{6}T^{-2} = \delta^{18}O_{kaolinite} - 0.1250x\delta^{2}H_{kaolinite} + 7.0375 \quad \text{(S7).}$$

The analogous derivation holds for smectite[47].

II. Approximation of $1000\ln\alpha = \delta_{clay} - \delta_{sw}$

A commonly used assumption to simplify mathematical operations in isotope geochemistry is that $1000\ln\alpha$ is the difference between two phases. In the case of clay mineral thermometry this approximation is between the clay mineral and the source water (equations 7 and 8). This approximation breaks down at extremely large fractionation factors (i.e. >100‰) because the mole fraction of the minor isotope is non-linear with the delta notation (as defined and used by the field; e.g., ref. 104). As such, the exact expression for the fractionation factor (α), based on the isotopic ratios (R) are described as:

$$^{18}\alpha_{kaol\text{-}water} = {}^{18}R_{kaol} / {}^{18}R_{sw} = (\delta^{18}O_{kaol} + 1000) / (\delta^{18}O_{sw} + 1000) \quad \text{(S8)}$$

$$^{2}\alpha_{kaol\text{-}water} = {}^{2}R_{kaol} / {}^{2}R_{sw} = (\delta^{2}H_{kaol} + 1000) / (\delta^{2}H_{sw} + 1000) \quad \text{(S9)}$$

As discussed in the main text $^{18}\alpha_{kaol\text{-}water}$ is greater than 1 and $^{2}\alpha_{kaol\text{-}water}$ is less than 1 resulting in clay minerals falling below and to the right of the GMWL or LMWL in $\delta^{18}O$-$\delta^{2}H$ crossplot space. In Figure S1 we demonstrate the consequence of this inaccuracy caused by the commonly used approximation by plotting clay lines produced from the precise expression (equations S8 and S9) versus the approximation (equations 7 and 8). Across Earth's surface temperatures and typical meteoric water values (Fig. S1A), inaccuracies in the calculated temperature are typically <2 °C, and are dependent on both the temperature of formation and the initial source water's isotopic composition (Fig. S1B).

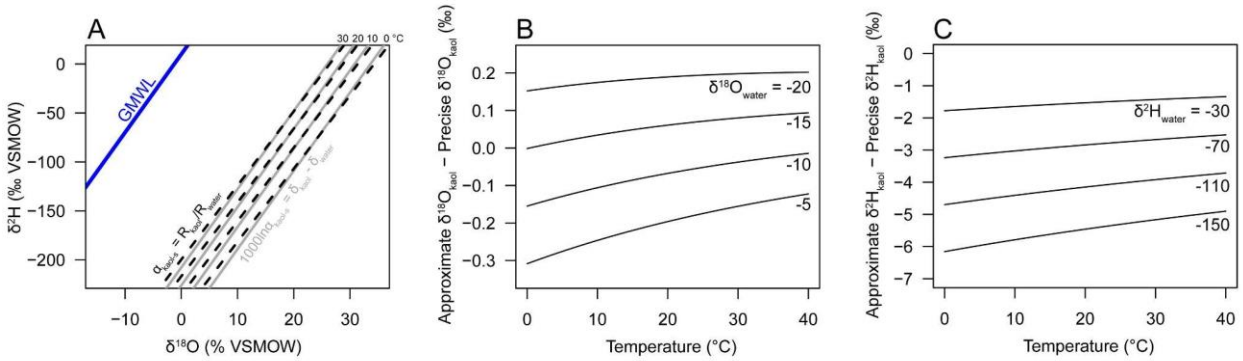

Figure S1. Sensitivity of calculations to $1000\ln\alpha = \delta_{clay} - \delta_{sw}$ approximation. **A)** Fractionation of global meteoric water line (blue line) to clay lines at 0 to 30 °C using the $1000\ln\alpha = \delta_{clay} - \delta_{sw}$ (as typically assumed; gray lines) compared to the precise definition for α (Equations 8 and 9). **B)** Difference between the approximate and precise fractionation formulations with respect to kaolinite $\delta^{18}O$ values for a given source water composition as a function of temperature. **C)** As in B) for $\delta^{2}H$.

III. Elaboration on assumptions and limitations

In the following sections we elaborate on a few assumptions and limitations associated with the effects described in the main text. We also provided additional contextual figures associated with the calculations.

Case 1. The role of seasonal co-variations of temperature and meteoric water isotopic composition

The amount and isotopic compositions of precipitation are known to display both positive and negative covariation with temperature depending on the region and season[53]. In tropical areas, a negative covariation tends to occur during monsoon rainfall due to the 'amount effect' (e.g., ref. 5). Mid- to high-latitudes, however, tend to exhibit positive covariation as factors such as moisture source, humidity, and temperature change[53]. Case 1 isolates the impact of these seasonal covariations on single-mineral clay thermometers without the inclusion of soil pore water evaporation or temperature variations (Figure S2).

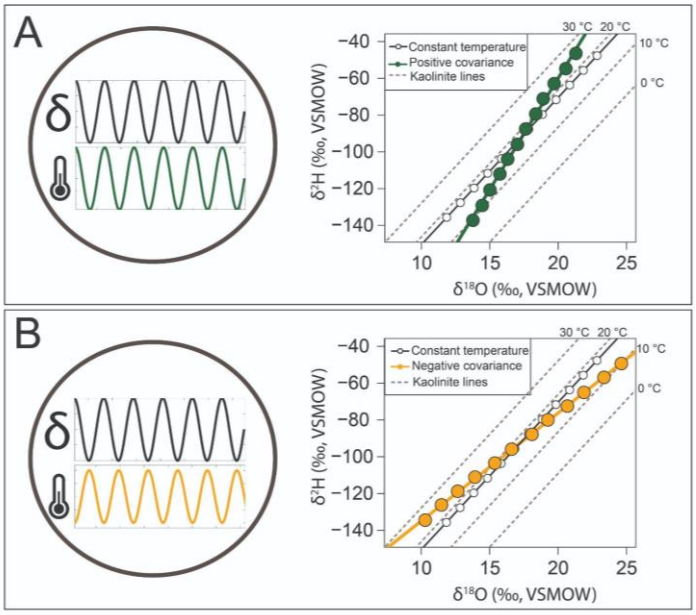

Figure S2. Impact of seasonal temperature variations of waters falling along the meteoric water line (MWL) on clay formation isotopic compositions as shown in Figure 1B. **A)** The case where precipitation isotopic compositions and monthly air temperatures are positively correlated. **B)** The case where precipitation isotopic compositions and monthly air temperatures are negatively correlated. Images in enclosed circles are illustrative depictions of the two cases. White circles in both panels represent the constant temperature case.

In Figure S3 we calculate the end-member evaporatively enriched waters (blue circles in Figure 1A) with positive and negative seasonality with respect to temperature variations. This does not yet resolve depth-dependent behavior but rather the maximum impact of surface temperature variations leading to changes in the clay line slope formed from evaporatively enriched waters. As in Figure S2 these assumed slopes are purely for illustrative purposes. With no seasonality of temperature imposed the result is that as water samples and the calculated clay line move away from the meteoric water line (i.e. have a lower d-excess value) the calculated clay values fall across the status quo contour lines (blue points, Figure 1A). Imposing a positive (negative) relationship between isotopic composition of precipitation and temperature results in steeping (shallowing) of slopes (green and orange points) rotated around the no temperature seasonality case. The trajectories shown in Figure 1C represent potential maximum cases, which if taken at face value with the status quo thermometry calculations would give temperatures dominantly less than freezing in the scenario described here. Incorporating the depth dependent trends in soil pore water stable isotopes and temperature fluctuations.

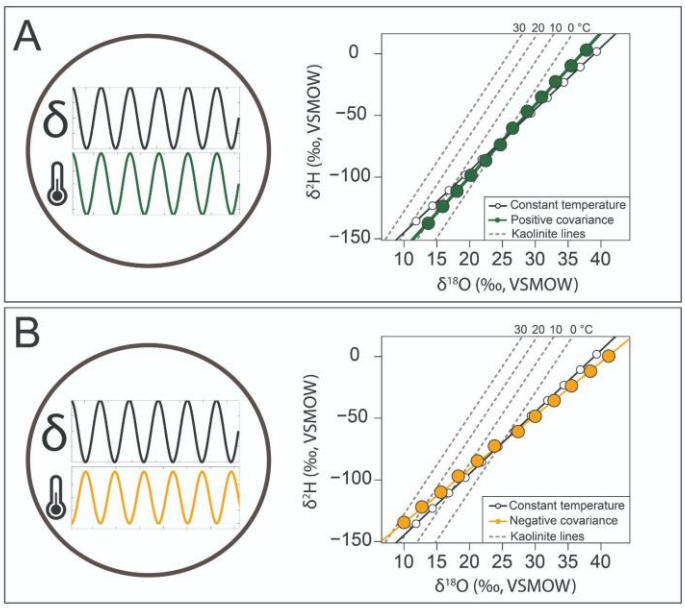

Figure S3. Impact of seasonal temperature variations of evaporated waters (see blue circles in Figure 1A of main text) on clay formation isotopic compositions. **A)** The case where precipitation isotopic compositions and monthly air temperatures are positively correlated. **B)** The case where precipitation isotopic compositions and monthly air temperatures are negatively correlated. Images in enclosed circles are illustrative depictions of the two cases. White circles in both panels represent the constant temperature case.

Case 2: The role of evaporatively enriched soil waters

For the purposes of determining the isotopic composition of soil minerals, as modeled in this work, this formulation does not account for the presence of the vapor phase in the upper most unsaturated zone in a soil that causes a decrease in $\delta^{18}O$ and $\delta^{2}H$ in the upper few centimeters[56, 57, 58]. It is most likely that a majority of clay mineral formation occurs below these depths [where evaporation predominates] based on weathering front profiles from chronosequences (e.g., ref. 74), justifying this simplifying assumption.

IV. Forward and inverse models

Forward model. We use measured modern soil pore water $\delta^{18}O$ and $\delta^{2}H$ ($\delta^{18}O_{sw}$ and $\delta^{2}H_{sw}$, respectively) as input to calculate $\delta^{18}O$ and $\delta^{2}H$ values of kaolinite ($\delta^{18}O_{kaol}$ and $\delta^{2}H_{kaol}$, respectively) as output. $\delta^{18}O_{sw}$ and $\delta^{2}H_{sw}$ are obtained from two published studies in Luquillo, Puerto Rico[66] and Corvallis, Oregon[67]. The results are visualized in Figure 2 of the main text. See MATLAB codes and pertinent input files used to calculate $\delta^{18}O_{kaol}$ and $\delta^{2}H_{kaol}$.

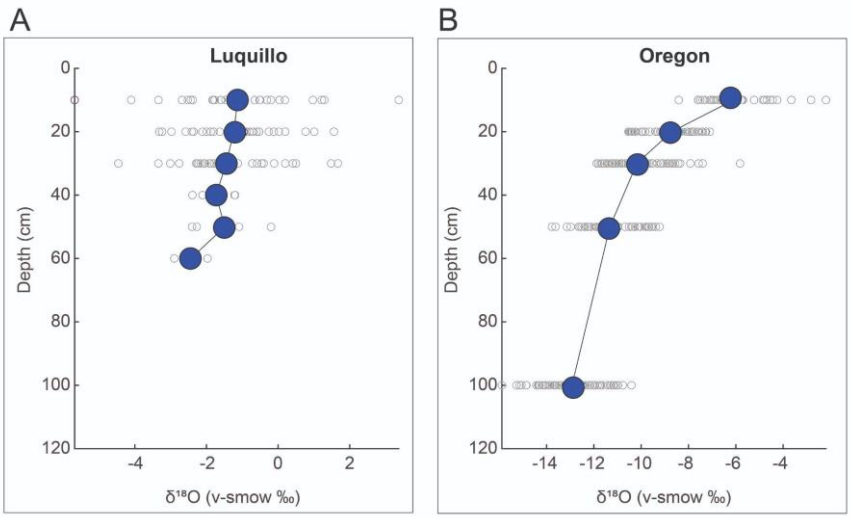

Figure S4. Soil pore water $\delta^{18}O$ depth profile for **A)** Luquillo and **B)** Oregon. Open gray circles represent pore water $\delta^{18}O$ data with depth. Filled circles represent corresponding mean values, connected by a line for emphasis. Note that the scales on the x-axis are not the same for both plots.

We underline a caveat in interpreting the Luquillo and Oregon soil pore water datasets. Figure S4 shows an apparent depth trend in the Oregon dataset. That is, soil pore water $\delta^{18}O$ decreases exponentially with depth. An empirical fit to the data (fit not shown) is approximated by a two-parameter exponential regression (R^2 0.994, RMSE 3.11). A decrease in soil pore water $\delta^{18}O$ with depth is a relatively common observation in settings with pronounced seasonality (e.g., ref. 105) and in soils undergoing evaporation[58]. The site in Oregon is in a Mediterranean climate with relatively strong precipitation and temperature seasonality. In kaolinite (clay formation) space (see Figure 2D in main text), the apparent depth trend at Oregon manifests as warmer clay formation temperatures closer to the surface, except at 10 cm. No such apparent depth trend exists in the Luquillo dataset, perhaps because Luquillo is considerably less seasonal than Oregon, or other sites where isotopic depletion of soil pore water with depth has been documented.

Another caveat that we underline in interpreting the Luquillo and Oregon soil pore water datasets is that our work assumes fidelity of soil pore water extraction techniques. Pore waters from both Luquillo and Oregon soil samples were reported to have been extracted using cryogenic vacuum distillation (CVD) technique[106]. In laboratory spiking experiments that subjected soils to extended high-temperature oven drying, some researchers have raised potential issues associated with the CVD technique's ability to extract the 'true' soil pore water isotopic compositions[107-109]. Other researchers, however, have questioned the transferability of findings from laboratory experiments to soils under natural conditions. For example, ref. 110 and 111 showed that in field studies whereby soils have not been subjected to the same conditions, the CVD technique could reliably reproduce the isotopic compositions of the original source water. In light of the ongoing debate in the literature regarding the fidelity of the CVD technique,

our work assumes that CVD is a reliable extraction technique for field soils, consistent with the determination made by ref 110.

Finally, we calculate depth-associated soil temperatures using Hillel's heat diffusion equation that includes a sinusoidal term, accounting for seasonal temperature fluctuations (ref. 64; Equation 6 in main text). For Luquillo, we use wet and dry season air temperatures of 26.8 and 25.1 °C, respectively [the two sampling points in ref. 66], as inputs to model the soil temperatures at corresponding $\delta^{18}O_{sw}$ and $\delta^{2}H_{sw}$ sampling depths. For Oregon, we use the mean annual temperature of 8.7 °C. Given that modeling $\delta^{18}O_{kaol}$ and $\delta^{2}H_{kaol}$ is sensitive to temperature (Equations S4 and S5), we emphasize that our assumptions that go into calculating depth-associated soil temperatures[64] are general approximations that may not be realistic (Figure S5). In the absence of measured soil temperatures with depth, our approach here must be treated purely as a first-order approximation. Future work could focus on *in situ* measurements of soil temperature at various depths in the soil profile.

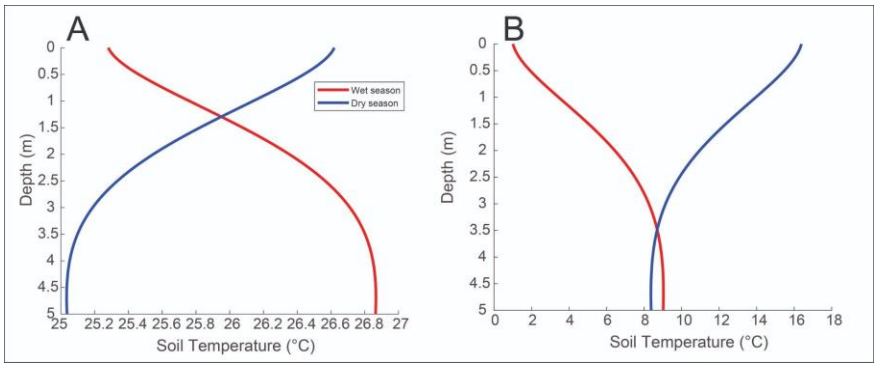

Figure S5. Modeled soil temperature profiles at respective sites in **A)** Luquillo and **B)** Oregon.

Inverse model. We use $\delta^{18}O_{kaol}$ and $\delta^{2}H_{kaol}$ data to predict the plausible values of $\delta^{18}O_{sw}$ and $\delta^{2}H_{sw}$ that best explain the observed kaolinite observations. $\delta^{18}O_{kaol}$ and $\delta^{2}H_{kaol}$ are obtained from two published studies in Finland[21] and the Sierras in western United States[29]. The results are visualized in Figure 3 of the main text. See MATLAB codes and pertinent input files used to calculate $\delta^{18}O_{sw}$ and $\delta^{2}H_{sw}$.

To model $\delta^{18}O_{sw}$ and $\delta^{2}H_{sw}$ using measured $\delta^{18}O_{kaol}$ and $\delta^{2}H_{kaol}$ (Equations S4 and S5), several soil temperature values were assumed. The solutions to the inverse problem are constrained by the relatively well-constrained physics of covariations on or below the LMWL (alternatively, GMWL). That is, $\delta^{18}O_{sw}$ and $\delta^{2}H_{sw}$ plotting 'on' the LMWL, by definition, approximate meteoric water isotopic compositions. Whereas, $\delta^{18}O_{sw}$ and $\delta^{2}H_{sw}$ plotting 'below' the LMWL indicate evaporative isotopic enrichment. We therefore consider as unrealistic any calculated $\delta^{18}O_{sw}$ and $\delta^{2}H_{sw}$ that fall 'above' the LMWL, which would otherwise represent the isotopic composition of the evaporate.

In Figure S6A, we see that if we assume a soil temperature of ~11 °C (which is similar to the long-term average air temperature of Auburn, CA), the modern soil pore waters are shown

to be above the LMWL on the 'evaporate space'. On the other hand, assuming a soil temperature of 50 °C shows that the soil pore waters are too enriched due to evaporation. Such a temperature would be unreasonably warm even for Eocene hothouse conditions (cf. ref. 29). However, if we assume a soil temperature of 33 °C, the soil pore waters plot close to the LMWL. We consider this to be more realistic than the other two extreme temperatures. Nevertheless, some data points still plot on the evaporate space (Figure S6B). We assume that these points are unrealistic values from which kaolinite would have formed. Thus, considering only the data points that plot on or below the LMWL, we determine the source waters of each modeled soil pore water (Figure S6C). That is, the meteoric water from which the clay mineral would have formed.

In tracing the source water isotopic composition, we assume that each calculated soil pore water must have evaporated along a soil evaporation line (SEL), following the approach of ref. 44. Figure S6C assumes an SEL slope of 3, close to the slopes of between 2 and 3 reported by ref. 112, and 3.1-3.4 reported by ref. 44. The approach of ref. 44 is a departure from the 'trendline approach' of earlier studies[113-117], which assumed that all evaporated waters originate from a single source water. The trendline approach is represented by the dashed black line in Figure S6C. In the absence of *a priori* and/or plausible information to inform an assumption that all evaporated soil pore waters originate from a single source water, we follow the mechanistic and more plausible approach of ref. 44.

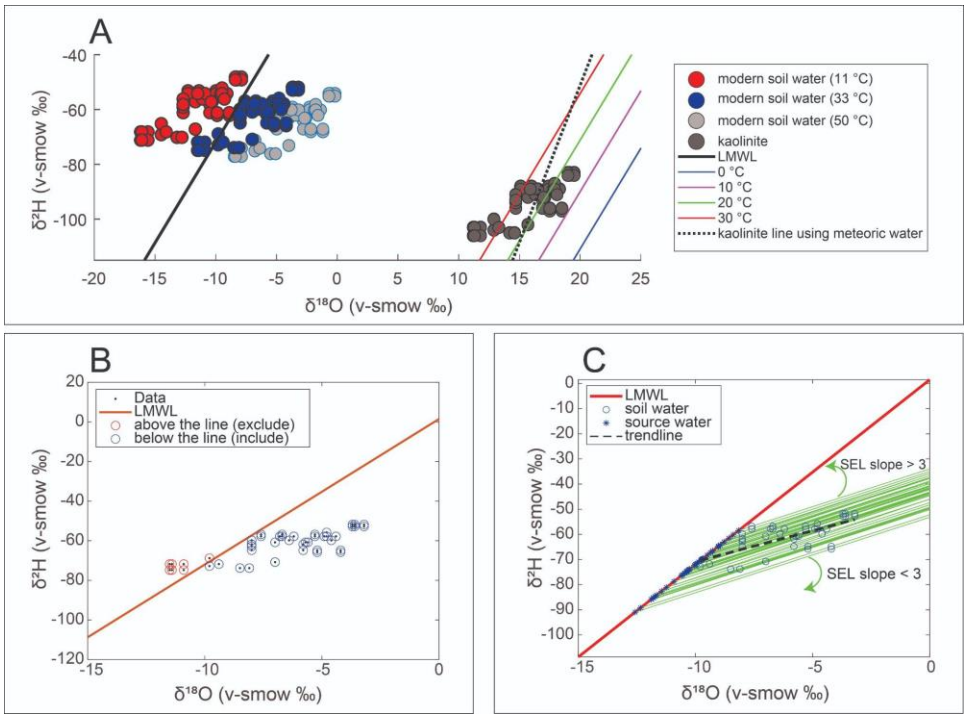

Figure S6. Determining source water isotopic compositions. **A)** Sensitivity of modeled $\delta^{18}O_{sw}$ and $\delta^{2}H_{sw}$ to various temperature assumptions (11, 33, 50 °C). **B)** Any calculated $\delta^{18}O_{sw}$-$\delta^{2}H_{sw}$ pair that plots above the LMWL are excluded from the determination of source water isotopic compositions. **C)** Tracing source water isotopic compositions as the intersection between the

soil evaporation line and the LMWL, constrained by the soil evaporation line (SEL) slope (here set at 3). The effects of SEL slopes greater than or less than 3 are represented by the direction of the green arrows. The 'trendline approach' is represented by the dashed black line (slope = 2.5 ±0.4 s.e.).

However, we want to emphasize that there are limitations to our inverse modeling approach. One of these limitations is that it assumes all soil pore waters in the dataset evaporated along a fixed SEL slope, which may be too simplistic. In reality, the conditions affecting each evaporated sample are likely to vary temporally (e.g., temperature and humidity), resulting in variable SEL slopes. Another limitation to our approach is that it mainly relies on uniform changes in temperature (Equations S4 and S6). In reality, other factors such as relative humidity above the evaporating surface and seasonal changes in precipitation amount and isotopic composition (e.g., Figures S2 and S3) are also likely to play a role in the degree of evaporative fractionation[7, 44, 53].

Table S1. Forward model. Sources of input datasets, input files, and MATLAB model parameters.

Model input	Notation in code	Description	Data source
Luquillo_forward.csv	-	n x 4 table: depth (in cm), soil temperature in °C, $\delta^{18}O_{sw}$ and $\delta^{2}H_{sw}$	1) depth, $\delta^{18}O_{sw}$ and $\delta^{2}H_{sw}$ from ref. 66 2) soil temperature (see next row)
Luquillo_precip.csv	-	n x 3 table: meanTp (in °C), $\delta^{18}O_{p}$ and $\delta^{2}H_{p}$	see next rows
Oregon_forward.csv	-	n x 4 table: depth (in cm), soil temperature in °C, $\delta^{18}O_{sw}$ and $\delta^{2}H_{sw}$	1) depth, $\delta^{18}O_{sw}$ and $\delta^{2}H_{sw}$ from ref. 67 2) soil temperature (see next row)
Oregon_precip.csv	-	n x 3 table: meanTp (in °C), $\delta^{18}O_{p}$ and $\delta^{2}H_{p}$	see next rows
Air temperature	meanTp	long-term mean monthly air temperature Luquillo site Sabana, 2002-2008 Oregon site GSWS10, 1999-2019	Scatena, F., IITF (2020). LCZO -- Meteorology, Air Temperature -- Daily -- Luquillo Mountains -- (2002-2009), HydroShare Gregory, S.; Johnson, S. 2019. Stream and air temperature data from stream gages and stream confluences in the Andrews Experimental Forest, 1950 to present
Soil temperature Luquillo wet and dry season air temp: 26.8 and 25.1 °C, respectively Oregon: mean annual air temp of 8.7 °C	soilT	modeled depth-associated soil temperature following Hillel (1982); see Equation 6	Model values based on input air temperature (meanTp) data
$\delta^{18}O_{sw}$ and $\delta^{2}H_{sw}$	d18O_soil d2H_soil	measured soil pore water isotopic compositions	Luquillo: Evaristo et al. (2016) Oregon: Brooks et al. (2010)
$\delta^{18}O_{p}$ and $\delta^{2}H_{p}$	d18Op d2Hp	amount-weighted monthly d18O and d2H of precipitation Luquillo Mountains (sites LQR3, LQR4,	Luquillo: U.S. Geological Survey Open-File Report 2014–1101, http://dx.doi.org/10.3133/ofr20141101

Model input	Notation in code	Description	Data source
		LQR5, LQR6) Oregon site PRIMET, 2014-2018	Oregon: Segura, C. 2022. Water stable isotopes for streams and precipitation samples in the HJ Andrews Experimental Forest and Mary's River Watershed, 2014-2018. Long-Term Ecological Research. Forest Science Data Bank, Corvallis, OR.

Table S2. Inverse model. Sources of input datasets, input files, and MATLAB model parameters.

Model input	Notation in code	Description	Data source
Finland_inverse.csv	-	n x 2 table: $\delta^{18}O_{kaol}$ and $\delta^{2}H_{kaol}$	From ref 19
Finland_precip.csv	-	n x 3 table: meanTp (in °C), $\delta^{18}O_{p}$ and $\delta^{2}H_{p}$	see next rows
Sierras_inverse.csv	-	n x 2 table: $\delta^{18}O_{kaol}$ and $\delta^{2}H_{kaol}$	From ref. 29, 83
Sierras_precip.csv	-	n x 3 table: meanTp (in °C), $\delta^{18}O_{p}$ and $\delta^{2}H_{p}$	see next rows
Air temperature	meanTp	long-term mean monthly air temperature Finland site Sodankylä, 1991-2021 Sierras site Auburn, Ca 1951-2010	Finland: Climate-data.org Sierras: UCANR IPM
Soil temperature	soilT	modeled depth-associated soil temperature following Hillel (1982); see Equation 6	Model values based on input air temperature (meanTp) data
$\delta^{18}O_{kaol}$ and $\delta^{2}H_{kaol}$	d18O_kaol d2H_kaol	measured kaolinite isotopic compositions	Finland: ref. 19 Sierras: ref. 29, 83
$\delta^{18}O_{p}$ and $\delta^{2}H_{p}$	d18Op d2Hp	amount-weighted monthly d18O and d2H of precipitation Finland: Rovaniemi station Sierras: Placer County	Finland: GNIP, Finland Rovaniemi station Sierras: OIPC calculator using geographic coordinates of Placer County, elevation 1292 ft (394 m)

References cited in supplemental text only

104. Brand, W. A., & Coplen, T. B. Stable isotope deltas: tiny, yet robust signatures in nature. Isotopes in environmental and health studies, 48(3), 393-409 (2012).

105. Goldsmith, G. R., Muñoz-Villers, L. E., Holwerda, F., McDonnell, J. J., Asbjornsen, H., & Dawson, T. E. (2012). Stable isotopes reveal linkages among ecohydrological processes in a seasonally dry tropical montane cloud forest. Ecohydrology, 5(6), 779-790.

106. West, Adam G., Shela J. Patrickson, and James R. Ehleringer. "Water extraction times for plant and soil materials used in stable isotope analysis." Rapid Communications in Mass Spectrometry: An International Journal Devoted to the Rapid Dissemination of Up-to-the-Minute Research in Mass Spectrometry 20.8 (2006): 1317-1321.

107. Orlowski, N., Breuer, L., & McDonnell, J. J. Critical issues with cryogenic extraction of soil water for stable isotope analysis. Ecohydrology, 9(1), 1-5 (2016).

108. Oerter, E., Finstad, K., Schaefer, J., Goldsmith, G. R., Dawson, T., & Amundson, R. (2014). Oxygen isotope fractionation effects in soil water via interaction with cations (Mg, Ca, K, Na) adsorbed to phyllosilicate clay minerals. Journal of Hydrology, 515, 1-9 (2014).

109. Meißner, M., Köhler, M., Schwendenmann, L., Hölscher, D., & Dyckmans, J. Soil water uptake by trees using water stable isotopes (δ 2 H and δ 18 O)− a method test regarding soil moisture, texture and carbonate. Plant and soil, 376, 327-335 (2014).

110. Newberry, S. L., Nelson, D. B., & Kahmen, A. Cryogenic vacuum artifacts do not affect plant water-uptake studies using stable isotope analysis. Ecohydrology, 10(8), e1892 (2017).

111. Newberry, S. L., Prechsl, U. E., Pace, M., & Kahmen, A. Tightly bound soil water introduces isotopic memory effects on mobile and extractable soil water pools. Isotopes in Environmental and Health Studies, 53(4), 368-381 (2017).

112. Gibson, J. J., Birks, S. J., & Edwards, T. W. D. Global prediction of δA and δ2H-δ18O evaporation slopes for lakes and soil water accounting for seasonality. Global biogeochemical cycles, 22(2) (2008).

113. Evaristo, J., Jasechko, S., & McDonnell, J. J.. Global separation of plant transpiration from groundwater and streamflow. Nature, 525(7567), 91-94 (2015).

114. Hervé-Fernández, P., Oyarzún, C., Brumbt, C., Huygens, D., Bodé, S., Verhoest, N. E. C., & Boeckx, P. J. H. P. Assessing the ‘two water worlds’ hypothesis and water sources for native and exotic evergreen species in south-central Chile. Hydrological Processes, 30(23), 4227-4241 (2016).

115. Javaux, M., Rothfuss, Y., Vanderborght, J., Vereecken, H., & Brüggemann, N. Isotopic composition of plant water sources. Nature, 536(7617), E1-E3 (2016).

116. Dogramaci, S., Skrzypek, G., Dodson, W., & Grierson, P. F. Stable isotope and hydrochemical evolution of groundwater in the semi-arid Hamersley Basin of subtropical northwest Australia. Journal of Hydrology, 475, 281-293 (2012).

117. Telmer, K., & Veizer, J. Isotopic constraints on the transpiration, evaporation, energy, and gross primary production budgets of a large boreal watershed: Ottawa River basin, Canada. Global Biogeochemical Cycles, 14(1), 149-165 (2000).